PAPER

Check for updates

Influence of lung extracellular matrix from non-IPF and IPF donors on primary human lung fibroblast biology†

Mohammadhossein Dabaghi, [ID] [a] Ryan Singer,[a,b] Alex Noble,[a]
Aidee Veronica Arizpe Tafoya,[b] David A. González-Martínez,[c] Tamaghna Gupta,[b]
Cécile Formosa-Dague, [ID] [d] Ivan O. Rosas,[e] Martin R. Kolb,[a,f] Yaron Shargall,[g]
Jose M. Moran-Mirabal [ID] [b,c] and Jeremy A. Hirota [ID] *[a,b,f,h,i]

Fibrosis, a pathological hallmark of various chronic diseases, involves the excessive accumulation of extracellular matrix (ECM) components leading to tissue scarring and functional impairment. Understanding how cells interact with the ECM in fibrotic diseases such as idiopathic pulmonary fibrosis (IPF), is crucial for developing effective therapeutic strategies. This study explores the effects of decellularized extracellular matrix (dECM) coatings derived from non-IPF and IPF donor lung tissue samples on the behavior of primary human lung fibroblasts (HLFs). Utilizing a substrate coating method that preserves the diversity of *in situ* ECM, we studied both the concentration-dependent effects and the intrinsic biochemical cues of ECM on cell morphology, protein expression, mechanobiology biomarkers, and gene expression. Morphological analysis revealed that HLFs displayed altered spreading, shape, and nuclear characteristics in response to dECM coatings relative to control plastic, indicating a response to the physical and biochemical cues. Protein expression studies showed an upregulation of α-smooth muscle actin (α-SMA) in cells interacting with both non-IPF and IPF dECM coatings, that was more prominent at IPF dECM-coated surface. In addition, YAP localization, a marker of mechanotransduction, was also dysregulated on dECM coatings, reflecting changes in mechanical signaling pathways. Gene expression profiles were differentially regulated by the different dECM coatings. The developed dECM coating strategy in this work facilitates the integration of tissue-specific biochemical cues onto standard cell culture platforms, which is ideal for high-throughput screening. Importantly, it minimizes the requirement for human tissue samples, especially when compared to more sample-intensive 3D models like dECM-based hydrogels.

Introduction

Fibrosis is a pathological condition marked by the excessive build-up of extracellular matrix (ECM) components, leading to significant tissue scarring and subsequent impairment of organ function.[1,2] This detrimental process is a common endpoint in chronic inflammatory diseases, particularly affecting the lungs in conditions like idiopathic pulmonary fibrosis (IPF).[3,4] Investigating the interactions between cells and the ECM is crucial for developing advanced *in vitro* models that can be used to test unexplored therapeutic approaches.[5,6] The ECM is an intricate assembly of proteins and glycoproteins, providing not only structural support to cells but also critical biochemical and mechanical (physical) signals that direct numerous cellular activities.[7] In a healthy state, the ECM plays a key role in guiding cellular proliferation, differentiation, and migration.[8] However, during fibrosis, the ECM is profoundly altered in both composition and physical properties, disrupt-

[a]Firestone Institute for Respiratory Health – Research Institute of St. Joseph's, Hamilton, ON L8N 4A6, Canada. E-mail: hirotaja@mcmaster.ca
[b]School of Biomedical Engineering, McMaster University, Hamilton, ON, L8S 4K1, Canada
[c]Department of Chemistry and Chemical Biology, McMaster University, Hamilton, ON, L8S 4M1, Canada
[d]TBI, Université de Toulouse, INSA, INRAE, CNRS, 31400 Toulouse, France
[e]Department of Medicine, Baylor College of Medicine, Houston, Texas, 77030, USA
[f]Division of Respirology, Department of Medicine, McMaster University, Hamilton, ON, L8N 4A6, Canada
[g]Department of Surgery, McMaster University, Hamilton, ON, L8S 4K1, Canada
[h]Division of Respiratory Medicine, Department of Medicine, University of British Columbia, Vancouver, BC, V6H 3Z6, Canada
[i]Department of Biology, University of Waterloo, Waterloo, ON, N2L 3G1, Canada
†Electronic supplementary information (ESI) available. See DOI: https://doi.org/10.1039/d4bm00906a

ing typical cell functions and leading to a state of persistent, abnormal repair.[5] Human lung fibroblast cells (HLFs) are integral to lung ECM remodeling and are key players in the development and progression of fibrotic conditions.[7] These cells respond adaptively to the varied cues presented by the ECM, significantly influencing the pathogenesis of fibrosis. A deep understanding of how HLFs interact with different ECM components, particularly under fibrotic conditions, is essential for unraveling the underlying mechanisms of fibrotic diseases and for creating biomaterials that can recapitulate the ECM characteristic of healthy and diseased states.[7,9]

Mechanical and biochemical signals are pivotal in shaping cellular behavior, affecting a wide range of activities from cell structure and movement to growth and specialization.[10,11] The physical characteristics of a cell substrate, including stiffness and topography, as well as its biochemical makeup, such as protein composition and presence of growth factors, are integral in determining cell biology.[12] Cells interact with these mechanical aspects of their external environment *via* focal adhesions and the cytoskeleton, engaging in a process known as mechanotransduction.[13] On stiffer substrates, cells tend to exhibit increased spreading, more robust stress fiber formation, and elevated traction forces.[7] This active mechanical engagement not only shapes cell structure but also influences signaling pathways, gene expression, and cell differentiation.[9] For instance, variations in substrate stiffness have been linked to different cell lineage paths in stem cell differentiation, with softer matrices favoring adipose cell lineage and stiffer ones leaning towards bone cell lineage.[14,15] Similarly, the ECM's biochemical signals, including specific proteins and growth factors, interact with cell surface receptors, initiating signaling pathways that impact cell adhesion, migration, survival, and even programmed cell death.[16,17] These intricate interactions dictate the cell sensitivity to both mechanical and biochemical stimuli in their environment.

Research into substrates with diverse mechanical properties has shed light on cell behavior, particularly in the context of HLFs.[18,19] It has been observed that substrates mimicking the stiffness of normal lung tissue support non-pathological behaviors in HLFs, while those emulating the stiffer, fibrotic lung tissue can induce pathologic changes in these cells, such as elevated alpha-smooth muscle actin (α-SMA) expression and increased ECM production.[19,20] This shows the critical role of mechanical cues in disease processes like fibrosis and points to potential strategies for managing or understanding such conditions. Various innovative materials and methods have been developed to create substrates with adjustable stiffness, including hydrogels that can be finely tuned and micro- and nanoscale patterned surfaces to provide precise mechanical stimuli.[20,21] These advances have deepened our understanding of how cells perceive and respond to their mechanical environment and have broadened the potential for creating more effective biomaterials for tissue engineering and disease modeling. In essence, the combination of mechanical and biochemical cues is fundamental to guiding cellular behavior, with the mechanical properties of the substrate potentially

being particularly influential.[11] The exploration of substrates with a range of mechanical characteristics has enriched our understanding of cell–material interactions, particularly for HLFs and fibrotic conditions, offering opportunities for future therapeutics developments and regenerative medicine approaches.

Many studies have explored the influence of substrate stiffness on HLF functions. Marinković *et al.* examined the influence of substrate stiffness on fibroblasts derived from non-IPF and IPF lungs, focusing on contractile and proliferative behaviors.[22] They found that IPF fibroblasts differ in their response to substrate stiffness changes compared to normal fibroblasts, with these differences diminishing in softer substrates. This research also showed that reducing substrate stiffness or inhibiting Rho kinase decreases the contractile function of IPF fibroblasts, suggesting that mechanical environment changes are key to controlling IPF fibroblast functions and could lead to new treatment approaches.[22] Blokland *et al.* revealed that increased stiffness in the ECM significantly affects senescence and fibrosis markers in HLFs.[23] HLFs grown on stiffer hydrogels demonstrated increased Yes-associated protein-1 (YAP) nuclear translocation and content, elevated RANKL secretion, and decorin protein accumulation. They also showed an upregulation of fibrosis-related genes like *ACTA2*, *COL 1A1*, and *Fbln1*, with more Fbln1 protein deposition. These findings suggested that a stiffer ECM prompts a response in HLFs that may amplify fibrotic progression through a cycle of increased fibrotic and senescence-associated factors.[23] Asano *et al.* demonstrated that changes in substrate stiffness affect HLF characteristics, revealing that fibroblasts on stiffer substrates tend to be more elongated and exhibit higher α-SMA expression and enhanced mobility. This variation was achieved using polyacrylamide hydrogels coated with collagen type I, representing a range of stiffness from 1 kPa to 50 kPa. The increased stiffness of the culture substrate was found to have a notable impact on HLF biology.[24] Enhanced movement was confirmed through various migration assays. Reducing α-SMA levels led to decreased fibroblast migration, indicating the role of stiffness in fibroblast activity and potential role in pulmonary fibrosis progression.[24] These studies highlight the critical role of substrate stiffness in HLF biology, suggesting the importance of integrating cell biology with materials science to explore novel therapeutic approaches for fibrotic diseases.

Hydrogels made of solubilized decellularized extracellular matrix (dECM) have risen as a prominent scaffold-based biomaterial that closely mimics the native ECM's composition and structure.[25] Retaining many of the biological properties of the natural ECM, dECM provides an ideal platform for examining cell–ECM interactions and understanding underlying mechanisms.[26] In the study conducted by Nizamoglu, an *in vitro* model was created to simulate fibrotic lung conditions by applying ruthenium/sodium persulfate crosslinking to lung ECM-derived hydrogels, increasing stiffness and modifying viscoelastic properties while maintaining biochemical composition.[27] The crosslinked hydrogels induced myofibroblastic

differentiation in HLFs, marked by changes in morphology and α-SMA expression, without affecting viability. This method highlights a novel approach to studying the mechanical impact of fibrosis on HLFs while preserving peptide components within the ECM.[27] In another work, Davila *et al.* investigated HLFs behavior in dECM hydrogels derived from IPF donor lung samples, demonstrating that hydrogel contraction is influenced by cell density and ECM protein concentration, with IPF fibroblasts showing heightened contraction.[28] The fibroblasts displayed reduced activation and altered expression of *COL1A1*, *ACTA2*, and *CTGF* in 3D dECM hydrogels, indicating a deviation from the myofibroblast phenotype. Additionally, IPF fibroblasts exhibited a proinflammatory state in the hydrogels, affecting cytokine expression and influencing immune cell responses in co-culture experiments. These findings highlight how hydrogel properties may induce a distinctive, more inflammatory fibroblast state, emphasizing the ECM's role in fibrosis and suggesting a need for physiologically accurate hydrogel models for better antifibrotic therapeutic development.[28] Such studies employing dECM-based hydrogels or scaffolds from both healthy and IPF tissues reveal that the tissue source is crucial in dictating fibroblast behavior, underscoring the importance of tissue origin in the development of fibrosis models and treatment strategies.

In this study, we have developed a coating strategy that integrates non-IPF and IPF dECM onto conventional cell culture plates, creating a system amenable to high-throughput analyses. By solubilizing the lung dECM and depositing it onto tissue culture plastic (TCP), we aimed to preserve disease-relevant biochemical cues while maintaining a scalable workflow. This approach allowed us to explore how varying the amount of deposited dECM (100 μg ml^{-1} *vs.* 1000 μg ml^{-1} nominal concentrations) influences surface topography, stiffness, and the subsequent cellular responses of primary HLFs. Using AFM under hydrated conditions, we characterized these coatings—revealing differences in surface topography, thickness, and stiffness between non-IPF and IPF dECM—thereby confirming that the source of ECM can impart distinct biophysical cues. Importantly, our cell response data suggest that IPF-derived dECM, particularly at the high concentration (1000 μg ml^{-1}), can have inhibitory effects on normal lung fibroblasts, a phenomenon not observed at the low concentration (100 μg ml^{-1}). These findings highlight how the dECM source (non-IPF *vs.* IPF) remains a key driver of pathological cues, with concentration serving as an additional parameter that modulates ECM–cell interactions. Overall, this work shows a high-throughput-compatible method for studying dECM-based disease modeling, with implications for investigating IPF and other fibrotic disorders *in vitro*.

Materials and methods

Decellularization of human lung tissues

We implemented a decellularization technique that was detailed in an earlier publication as depicted in Fig. 1.[26] All experiments were performed in accordance with the Tri-Council Policy Statement: Ethical Conduct for Research Involving Humans (TCPS 2) and other applicable regulations. The study was approved by the Hamilton Integrated Research Ethics Board (HiREB – 5305-T), which provides ethical review and oversight on behalf of Hamilton Health Sciences, St. Joseph's Healthcare Hamilton, Research St. Joseph's-Hamilton, the Faculty of Health Sciences at McMaster
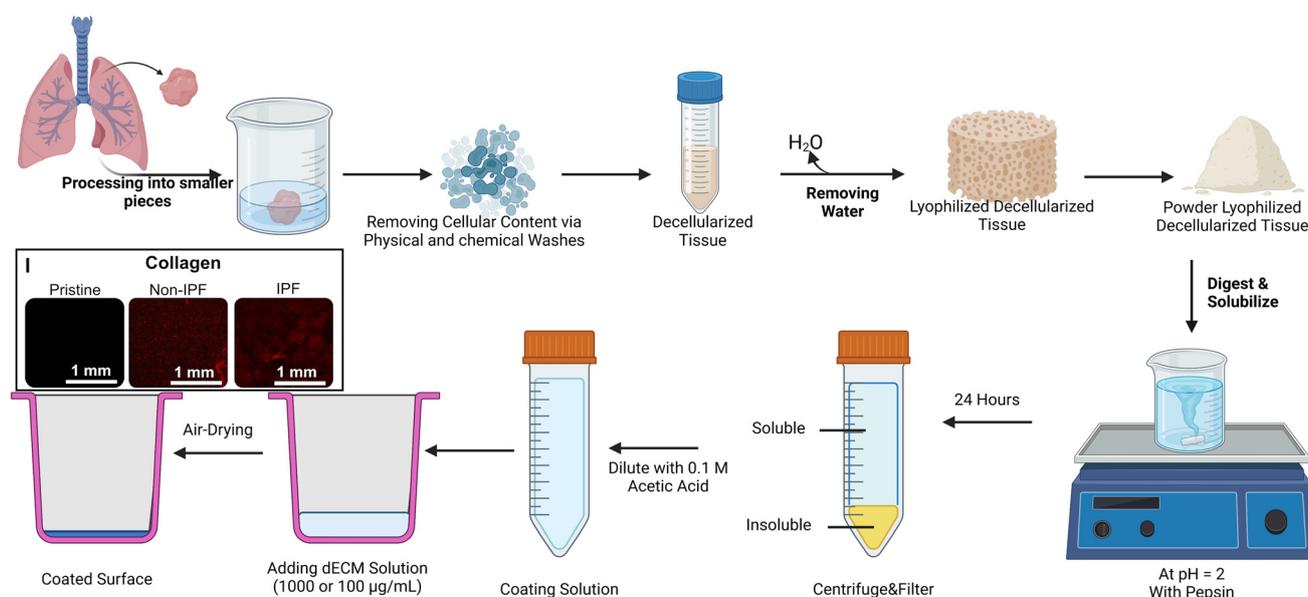

Fig. 1 The decellularization process of human lung tissues from non-IPF and IPF donors and the coating process for deposition of the solubalized dECM. (I) Immunofluorescence staining of collagen type I after coating the plates with non-IPF and IPF dECM confirming the successness of ECM's proteins depositions. Created in Biorender.com.

University, and Niagara Health. HiREB operates in compliance with the International Conference on Harmonisation of Good Clinical Practices Guideline (ICH GCP), Part C Division 5 of the Food and Drug Regulations, Part 4 of the Natural Health Products Regulations, Part 3 of the Medical Devices Regulations, and the Ontario Personal Health Information Protection Act (PHIPA) 2004 and its applicable regulations. Participants provided informed consent, and lung tissue samples were obtained during routine lung surgeries as part of their medical treatment. Residual tissues deemed unnecessary for clinical diagnosis were allocated to our laboratory. These tissues were promptly flash-frozen using liquid nitrogen and stored in a liquid nitrogen tank. Both non-IPF and IPF samples were thawed overnight in the refrigerator before decellularization. After thawing, the tissues were cut into 1 cm segments using surgical instruments. These segments were subsequently divided into smaller pieces, approximately 2–3 mm in size and added to the 5 ml volume mark in a 50 ml centrifuge tube. Each tube was subsequently filled with approximately 35 mL of the specified reagent (for a total volume of 40 mL).

Up to 5 mL of lung tissue was allocated to each 50 mL Falcon tube. When multiple tubes were necessary due to the sample's volume, care was taken to distribute the tissue equally across tubes, as any variation could influence the effectiveness of the decellularization process. Each tube was then filled to 40 mL with the appropriate reagent for that specific decellularization step, such as PBS or Triton X-100 (Sigma Aldrich, Canada, Catalog number: T9284-500 ml), ensuring the tissue volume remained under 5 mL. Tubes were subsequently treated with 0.1% Triton X and agitated on a rocker/nutator for 30 minutes. Following agitation, the contents of the tubes were filtered through a 100 μm pore cell strainer (Falcon-352360-Yellow strainer, VWR, Ontario, Canada), with solids retained and the filtrate discarded within a biosafety cabinet. The tissue was then rinsed by adding phosphate-buffered saline (PBS) and agitating for another 30 minutes to remove traces of Triton X. The wash was repeated, and 2% sodium deoxycholate (SDC, Sigma Aldrich, Canada, Catalog number: D6750-100G), known for disrupting cellular structures, was added. The tubes were placed on a rocker/nutator and left to agitate at 4 °C overnight. The following day, SDC was strained out, and the tubes were refilled with PBS supplemented with 1% Antibiotic-Antimycotic solution antimycotic (ThermoFisher, Canada, Catalog number: 15240062), and agitated for 24 hours. During this period, the PBS was refreshed at least once. After this, autoclaved deionized water was used to rinse the samples for a minimum of two hours before replacing it with a 1 M sodium chloride (NaCl) solution to induce hypertonic conditions, agitated for 30 minutes. Post NaCl agitation, the tubes were washed with autoclaved DI water again for 30 minutes, followed by a 1% Triton X treatment for the same duration. Tubes were subsequently washed with PBS containing antibiotic-antimycotic for two to three days with PBS replacement two times per day. Once this was completed, the samples were rinsed with autoclaved DI water,

agitated briefly, and stored at −80 °C until lyophilization. The lyophilization was done using a Benchtop Freeze Dryer (FreeZone 2.5 Liter −84 °C, Labconco, freezing temperature ~−84 °C and vacuum pressure ~0.005 mbar). Once freeze-dried, the tissues were pulverized in a mortar with a pestle in the presence of liquid nitrogen to produce fine dECM powders. These powders were then refrigerated at 4 °C until needed for further experimental use.

dECM solubilization and cell culture surface coating

A solution was prepared by combining dECM powder at a concentration of 10 mg mL^{-1} with 0.1 N hydrochloric acid, with pepsin added at 1 mg mL^{-1} concentration to initiate digestion.[29] This mixture was continuously stirred between 300 and 500 RPM (Cimarec+™ Stirring Hotplates Series, ThermoFisher, Canada) for 24 hours at ambient temperature to ensure thorough digestion. Following this period, the solution was centrifuged at ~5000g for 12 minutes to separate the dissolved material from any undigested residue. The supernatant, containing the digested dECM, was then carefully pipetted into conical tubes, while the residual undissolved solids were discarded (Fig. 1). Subsequently, the collected supernatant solution was diluted with 0.1 N acetic acid to achieve desired concentrations. In addition, total protein assay and gel electrophoresis were conducted to quantify the amount of the total protein and other large protein distributions for both samples as shown in Fig. S1.†

Prior to adding the dECM solutions to plates for substrate coating, each plate was subjected to oxygen plasma treatment at 900 mTorr for two minutes (Harrick Plasma cleaner, Model: PDC-001-HP, Power: 45 W, Ithaca, NY, USA). Following this step, dECM solutions derived from either non-IPF or IPF sources, at concentrations of 100 μg mL^{-1} and 1000 μg mL^{-1}, were added to the wells of the plates (added volume to each well of 48-well plate was 1 mL). For specific experiments comparing coating materials, coatings of collagen (Rat Tail Collagen Solution, Acid Soluble, 4 mg mL^{-1}, Advanced Biomatrix, product number: 5056-20ML, Carlsbad, CA, USA) and Matrigel (Geltrex™ LDEV-Free Reduced Growth Factor Basement Membrane Matrix, product number: A1413201) were prepared at two concentrations (100 μg mL^{-1} and 1000 μg mL^{-1}) as controls, using a coating method proposed in this study. These plates were then stored at 4 °C overnight to facilitate the coating process. The next day plates were transferred to a biosafety cabinet and left exposed to air to allow evaporation of any residual water from the dECM solution. Once dry, the wells were washed gently with PBS twice to remove any unbound dECM. Finally, the plates were subjected to UV sterilization to ensure aseptic conditions before the seeding of cells.

After digestion, a known volume of both non-IPF and IPF dECM solutions was frozen at −80 °C overnight, lyophilized, and weighed to determine the digestion yield and the precise dry mass of the digested materials. For instance, in one experiment, both non-IPF and IPF dECM solutions contained 7 mL of solution, prepared at a concentration of 10 mg mL^{-1} dECM

and 1 mg mL^{-1} pepsin (approximately 1.1 wt%), equating to 70 mg of dECM per sample. Following digestion, approximately 2 mL of the solution was discarded, leaving 5 mL of solution for analysis. The final dry mass recovered from the IPF dECM solution was measured as ~50 mg, while the non-IPF dECM solution yielded ~48 mg. These values correspond to final concentrations of 1.22 ± 0.05 wt% ($n = 3$ − technical replicates) for the IPF dECM solution and 1.20 ± 0.03 wt% ($n = 3$ − technical replicates) for the non-IPF dECM solution. The nominal concentrations of 100 μg mL^{-1} and 1000 μg mL^{-1} were calculated based on the initial dECM mass, and these values approximate the weighed dry mass.

Surface analysis

For AFM analysis, high-temperature polyester sheets (McMASTER-CARR, Product Number: 8567K96, Elmhurst, IL, USA) with a thickness of 127 μm were cut into 15 mm diameter disks. The disks were rigorously washed with isopropanol overnight, rinsed with deionized (DI) water, and dehydrated in an oven at 75 °C. Prior to coating, the disks were activated using oxygen plasma treatment. Subsequently, the polyester disks were placed at the bottom of a 24-well plate, and the coating solutions were applied and left to dry in ambient conditions.

To prepare samples for AFM experiments, dECM coated disks were immersed in a PBS buffer solution at pH 7.4 overnight at 4 °C. After that, the PBS buffer was replaced by fresh PBS pH 7.4 at room temperature; the samples were then directly used in liquid conditions for AFM experiments.

For AFM imaging and roughness analysis, AFM height images of different areas were recorded using the Quantitative Imaging mode available on the Nanowizard IV XP AFM (Bruker, USA), with MLCT cantilevers (Bruker, nominal spring constant of 0.01 N m^{-1}). Images were recorded with a resolution of 150 × 150 pixels using an applied force comprised of 1 nN and a z-length of 1 μm. In all cases, the cantilever spring constants were determined using the thermal noise method prior to imaging.[30] Large-scale images on 10 × 10 μm areas were recorded to obtain a qualitative view of the samples, while small-scale images on 1 × 1 μm areas were recorded to perform roughness measurements. For this, these height images were analyzed using the data processing software (Bruker, USA) to determine the arithmetic average roughness (R_a). In each condition, 6 different images were recorded on 6 different areas for roughness analysis.

For nanoindentation experiments, the AFM was used in force spectroscopy mode using an applied force comprised between 1 and 3 nN depending on the sample tested, with MLCT cantilevers (Bruker, nominal spring constant of 0.01 N m^{-1}). Force maps of 20 × 20 pixels on 100 × 100 nm areas were recorded; 6 different areas were probed for each sample. Young's moduli were then calculated from 50 nm indentation curves using the Hertz model in which the force F, indentation (δ), and Young's modulus (Y_m) follow eqn (1), where α is the tip opening angle (17.5°), and v is the Poisson ratio (arbitrarily assumed to be 0.5). The cantilever spring constants were determined by the thermal noise method:[30]

$$F = \frac{2 \times Y_m \times \tan \alpha}{\pi \times (1 - v^2) \times \delta^2} \qquad (1)$$

Cell culture

Primary HLFs were extracted directly from non-IPF human lung tissue samples as reported in our previous work[26] and cultured in DMEM with 10% fetal bovine serum (FBS) (Wisent Inc., Saint-Jean-Baptiste, Canada, product number: 080-450) and 1% penicillin–streptomycin (Gibco, United States, Catalog number: 15140122). For each round of experiments, HLFs were extracted from 3 or 4 donor tissues and used in this study as replicates. HLFs were used within the first seven passages of culture in T75 or T175 Flasks. For experiments, HLFs were trypsinized and seeded into each well of the prepared 24-well plates or 48-well plates at a density of approximately 5 × 10^3 cells per cm^2 or 2 × 10^4 cells per cm^2. Initially, the cells were cultured in DMEM containing 10% FBS until they reached ~70% confluency, a state where sufficient cell coverage is achieved without overcrowding. Once the desired confluency level was attained, the cells were transitioned to serum-free DMEM for 24 hours prior to starting experiments for the high cell density. For the low cell density studies, cells were cultured for 48 hours without starvation.

Immunofluorescence staining

To perform nuclear staining of the fixed samples, NucBlue™ Live ReadyProbes™ Reagent (Hoechst 33342-Invitrogen, ThermoFisher, Canada, Catalog number: R37605) or DAPI was applied in accordance with the manufacturer's guidelines. The fixation process began with a double PBS wash, which was repeated between all subsequent staining steps. Samples were then incubated for 15 minutes with 10% buffered neutral formalin (Sigma Aldrich, Canada, Catalog number: HT501128-4L) to fix the cells. This was followed by a 10 minute permeabilization step involving 0.5% Triton X-100 to allow staining agents to access the cellular components. To minimize non-specific staining, the fixed and permeabilized samples were treated with a 3% bovine serum albumin (BSA) solution for 1 hour (Sigma Aldrich, Canada, Catalog number: A2153-50G). Afterward, the samples were incubated with primary antibodies diluted in 1% BSA for 24 hours at 4 °C, specifically targeting α-SMA with a monoclonal antibody (Sigma Aldrich, Canada, catalog number: A2547) and Yes-associated protein (YAP, Santa Cruz Biotechnology, Canada, catalog number: sc-101199). This step was followed by another 24 hour incubation at 4 °C with secondary antibodies, DAPI or Hoechst 33342, and Phalloidin-iFluor 594 (Abcam, Canada, catalog number: ab176757), all in 1% BSA, to enable multiple staining components to attach to specific cell structures.

Widefield fluorescence imaging of the cells was performed using a ThermoFisher EVOS M7000 microscope equipped with GFP, DAPI, and Texas Red filters. This setup facilitated the detailed visualization of the cells and their components, particularly the α-SMA expression and YAP localization. In detail, multiple images were taken for each sample from every donor

cell sample, and these images were then stitched using the microscope's software. The resulting tiled images were utilized to quantify the level of α-SMA expression and to determine the localization of YAP. The mean gray value or the integrated intensity values within the regions of interest was calculated using ImageJ[31] or Fiji[32] software. To analyze α-SMA expression, images were captured of the entire well area. Integrated intensity values of the cells were quantified after background subtraction from areas devoid of cells. These values were then normalized to the cell count, determined by enumerating the nuclei.

For detailed cell morphology assessment and YAP quantification, CellProfiler[33] software was used. For these analyses, instead of using tiled images, images from every field of view were used to enhance thresholding. The analysis identifies nuclei as primary objects and actin fibers or αSMA or YAP as secondary objects, which helps in defining cell boundaries and the cytoplasm. With this information, the cell-covered area, cell eccentricity, nucleus area, and nucleus eccentricity were evaluated. These values were averaged across multiple single images, and the averaged values were subsequently plotted in the final graphs.

For cell proliferation assessment, entire wells were scanned with a focus on the nuclei, using the number of nuclei as a proxy for cell count. This number was then normalized by the surface area of each well to calculate cell density. This method provides an efficient way to estimate cell proliferation rates and understand how cells are growing and responding in different experimental conditions.

Gene expression analysis

For RNA collection, cell samples were lysed using Buffer RLT and subsequently purified following the manufacturer's instructions utilizing RNeasy Mini Kit columns (Qiagen, Toronto, Ontario). Nanostring gene expression profiling was performed on the RNA extracted from HLFs cultured on both non-IPF and IPF-coated surfaces with pristine plastic controls.[34] A previously constructed Nanostring codeset panel for genes related to fibrosis was used. The pre-processing and normalization of this data was carried out using nSolver 2.5 software, available at **https://www.nanostring.com**. This process involved using four negative controls for background subtraction and four positive controls to facilitate normalization. Subsequently, a total counts normalization step was implemented.

Statistical analysis

GraphPad Prism 10 (GraphPad Software, United States) was the chosen software for generating graphs and performing statistical analyses in this study. The data were presented as mean values accompanied by standard errors of the mean to provide a clear and standardized measure of central tendency and variability. To statistically compare the means of multiple experimental groups, one-way ANOVAs were conducted along with Bonferroni corrections as a *post-hoc* test for multiple comparisons. This approach helps in controlling the overall type I error rate when conducting several pairwise tests. For scenarios where only two groups were compared, unpaired t-tests were utilized to determine the statistical significance between the group means.

Results

Surface analysis of dECM coatings

SEM imaging provided initial insights into the morphology of the non-IPF and IPF dECM-coated surfaces (Fig. S2A†). At a lower concentration (100 μg mL^{-1}), both non-IPF and IPF coatings exhibited microscale fibers, while at a higher concentration (1000 μg mL^{-1}), a thin yet more continuous film was observed, enveloping the substrate. Notably, the non-IPF-1000 surfaces displayed abundant, intertwined fibers, whereas IPF-1000 coatings appeared denser with fewer discernible fibers.

AFM topographical analysis (Fig. 2A) further confirmed the presence of fibrous structures on both non-IPF-1000 and IPF-1000 coatings, including fibers not readily visualized by SEM. Despite these morphological differences, quantification of surface roughness (Fig. 2B and C) revealed no statistically significant difference between the non-IPF-1000 and IPF-1000 groups. However, force indentation experiments (Fig. 2D and E) showed that non-IPF-1000 coatings (1020 ± 370 Pa) were stiffer than IPF-1000 (490 ± 240 Pa). At the lower coating concentration (100 μg mL^{-1}), roughness and stiffness were similarly indistinguishable between non-IPF and IPF coatings (Fig. S3†). To estimate coating thickness, an AFM scratch assay was performed by applying high force over a 1 μm × 1 μm area (Fig. S4†). At 100 μg mL^{-1}, the tip penetrated through the full thickness of both non-IPF and IPF coatings, reaching the underlying substrate and indicating approximate thicknesses of ~200 nm and ~400 nm, respectively. In contrast, at 1000 μg mL^{-1}, the probe did not reach the underlying substrate for either condition, suggesting that both non-IPF-1000 and IPF-1000 coatings exceed 1 μm in thickness.

Morphological responses of HLFs to dECM coatings

We next examined the morphological adaptations of HLFs to surfaces coated with dECM derived from non-fibrotic tissues. Morphological parameters including cell area, nucleus area, cell eccentricity, and nucleus eccentricity were measured to understand the influence of dECM coatings on cell and nuclear shape and size (Fig. 3A). The cell area measurements revealed that cells seeded on tissue culture plates (TCP) exhibited the largest surface area compared to all surfaces coated with dECM (Fig. 3B). No significant difference in cell area was observed between the two dECM concentrations (either non-IPF or IPF dECM). However, cells on IPF-1000 demonstrated a larger area than those on non-IPF-1000. Conversely, the average nucleus area showed an opposite trend: cells on TCP had the smallest nucleus area, while those on dECM-coated surfaces had larger nucleus areas, except for non-IPF-100 (Fig. 3C). There was no significant difference between the two dECM concentrations regarding nucleus area, but cells on IPF-100 exhibited a higher nucleus area compared to non-IPF-100. Cell eccentricity generally mirrored the pattern observed in cell area, with cells on TCP displaying higher eccentricity, indicating a more elongated
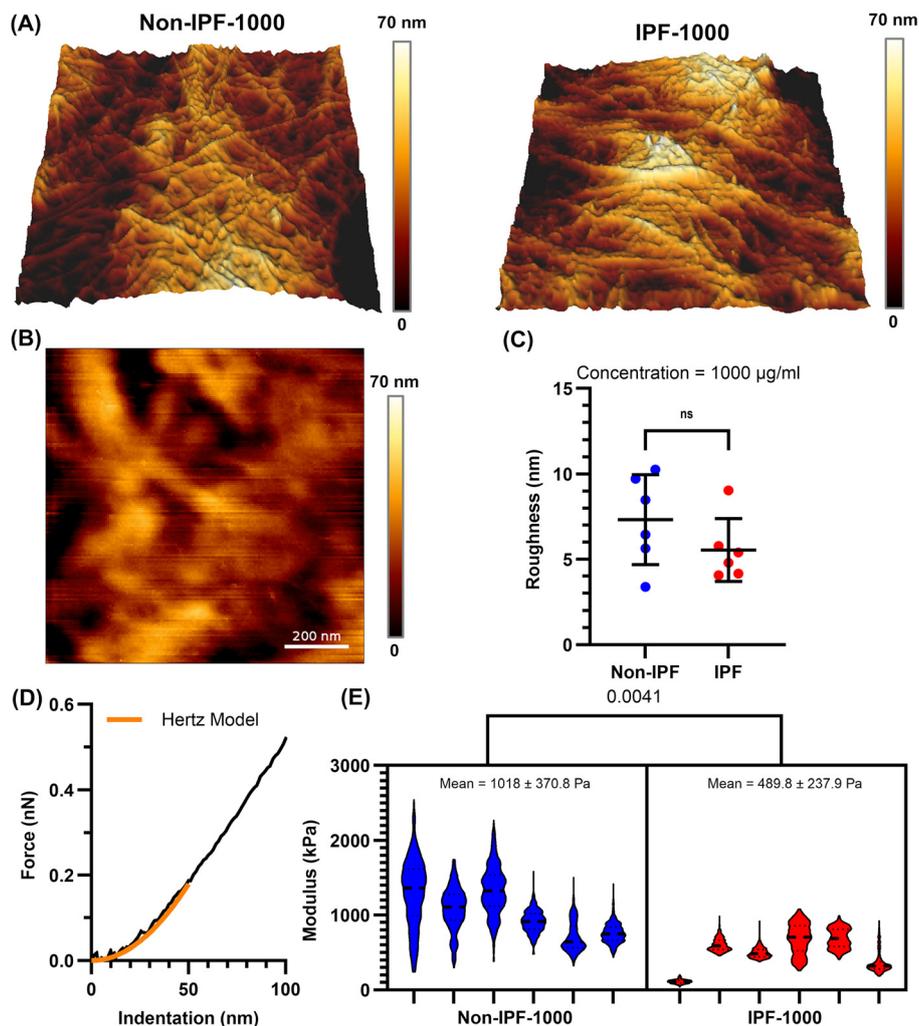
Fig. 2 AFM characterization of dECM deposited from high concentration dECM solutions (1000 μg mL^{-1}). (A) 3D visualization of topographical maps of Non–IPF and IPF dECM coatings. Imaged areas are 10 μm wide. (B) Representative topographical map of area used to acquire force curves (scale bar is 200 nm). (C) Comparison of film roughness. Values presented are mean and standard deviation of $n = 6$ independently imaged areas from $n = 3$ independently prepared replicate samples. (D) Sample force indentation curve and Hertz model fit to an indentation of 50 nm. (E) Violin plots for $n > 380$ force indentation curves in each of the $n = 6$ replicate areas scanned for each type of dECM coatings ($n = 3$ independently prepared replicate samples). Values represent mean and standard deviation calculated between the replicate area means.

shape (Fig. 3D). Cells on IPF-1000 had lower eccentricity than those on IPF-100. Lastly, nucleus eccentricity was similar across all conditions, except that cells on IPF-1000 exhibited lower nucleus eccentricity compared to those on TCP (Fig. 3E). These results present an overall analysis of HLF morphology in response to substrate differences, revealing that the physical and biochemical properties of dECM coatings can influence cell shape and nuclear characteristics, which are critical factors in understanding cell behavior and function.

Impact of dECM donor health status on HLF proliferation

We next investigated how dECM donor health status affects HLF proliferation. We compared cell proliferation across TCP, non-IPF lung tissue dECM coatings, and IPF lung tissue dECM coatings at both 100 and 1000 μg ml^{-1} concentrations (Fig. 4). Our findings indicated that dECM coatings derived from non-IPF

lung tissues promoted better cell adhesion and proliferation compared to the uncoated TCP, with no discernible difference between the two concentrations of non-IPF dECM. In contrast, cells seeded on IPF dECM coatings exhibited reduced proliferation rates, particularly at the higher concentration of 1000 μg ml^{-1}. This reduction was significant enough that the cell proliferation rate on 1000 μg ml^{-1} IPF dECM coating aligned closely with that on TCP. This suggests that the source of dECM —non-IPF *versus* IPF tissue—plays a critical role in affecting cell proliferation. Further, the observed differences between the 100 μg ml^{-1} and 1000 μg ml^{-1} concentrations of IPF dECM coatings suggest a concentration-dependent response in cells.

α-SMA expression in HLFs on dECM coatings

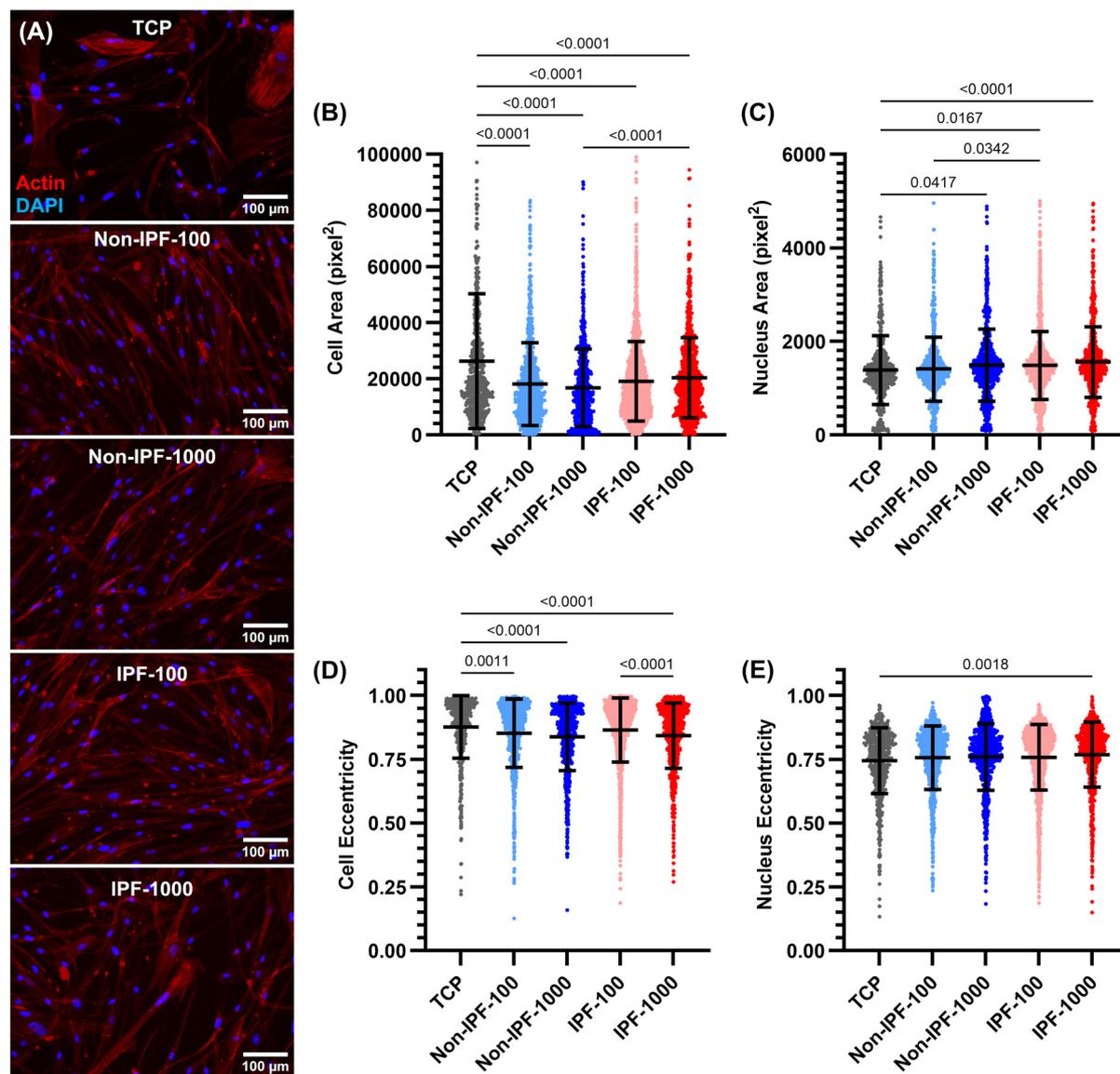We next investigated the expression of α-SMA in HLFs seeded on various surfaces, TCP and both non-IPF and IPF derived

Fig. 3 Morphological Evaluation of HLFs on dECM-Coated Surfaces compared to TCP using single cell analysis: (A) Representative images of HLFs stained with phalloidin to visualize actin fibers and DAPI for nuclei. The subsequent panels quantify changes in (B) cell area, (C) nucleus area, (D) cell eccentricity, and (E) nucleus eccentricity, assessing the impact of dECM coatings on cell morphology. $N = 4$. E Each data point represents an individual cell, with data collected from four independent donors. Statistical analysis was performed using the ordinary one-way ANOVA method.

dECM coatings at 100 and 1000 µg ml^{-1} concentrations. Cells were stained with DAPI for nucleus, phalloidin for F-actin fibers, and α-SMA (Fig. 5A), and the fluorescence intensity of α-SMA was quantified (Fig. 5B). Cells on IPF dECM coatings at the 1000 µg ml^{-1} concentration exhibited the highest α-SMA expression compared to all other conditions, including TCP (Fig. 5A and B). This finding is particularly noteworthy given that TCP, being a stiffer substrate, is typically expected to induce fibroblast-myofibroblast transition.[9] However, it appears that the surface modifications introduced by the dECM coatings, regardless of their source, have a more pronounced effect, leading to increased α-SMA expression.

The coatings at the lower concentration of 100 µg ml^{-1} also elevated α-SMA expression compared to TCP but to a lesser extent than the 1000 µg ml^{-1} dECM coatings from both non-IPF and IPF sources (Fig. 5A and B). As expected, IPF dECM at 100 and 1000 µg ml^{-1} induced higher α-SMA expression compared to the equivalent concentration of non-IPF dECM. However, non-IPF-1000 and IPF-100 caused the similar increase in α-SMA expression. These results suggest that α-SMA expression in HLFs may be influenced by both the physical changes to surface characteristics due to dECM coating and the biochemical nature of the dECM source.

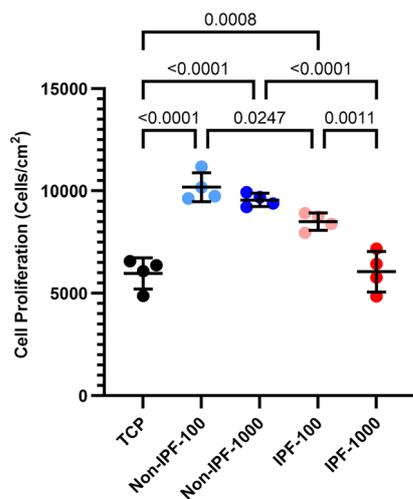To investigate whether the observed changes in α-SMA expression are specifically due to lung-derived dECM or merely

Fig. 4 HLFs proliferation on non-coated and coated surfaces. Cell nuclei were stained with DAPI followed by scanning of an entire well focused on the plane of nuclei, with the number of nuclei a proxy for cell count. This count was then normalized against the surface area of each well to accurately calculate the cell density. $n = 4$ experimental replicates with mean values presented with standard deviation. Ordinary one-way ANOVA was used for statistical analysis.

a result of applying any ECM coating, we incorporated additional coatings using collagen type I and Matrigel. Collagen type I, the most abundant ECM protein in most tissues, is widely utilized as an ECM coating to promote cell adhesion and proliferation. Matrigel, on the other hand, is a commercially available basement membrane matrix derived from Engelbreth-Holm-Swarm (EHS) mouse sarcoma. It is composed of a complex mixture of extracellular matrix proteins, including laminin, collagen IV, entactin, and heparan sulfate proteoglycans. This intricate composition makes Matrigel an excellent ECM coating material for replicating the natural cellular microenvironment, thereby supporting cell differentiation, growth, and migration.

Both collagen and Matrigel coatings were prepared at two concentrations—low (100 μg mL^{-1}) and high (1000 μg mL^{-1})—and compared to non-IPF and IPF dECM coatings, as illustrated in Fig. 6. Our results show that IPF dECM coatings, at both 100 μg mL^{-1} and 1000 μg mL^{-1}, significantly increased α-SMA expression in HLFs compared to the other conditions (Fig. 6A–D). In contrast, Matrigel coatings at both concentrations resulted in the lowest α-SMA expression, while non-IPF and collagen coatings induced similar levels of α-SMA expression in HLFs. These findings suggest that the enhanced α-SMA expression is associated with the specific biochemical
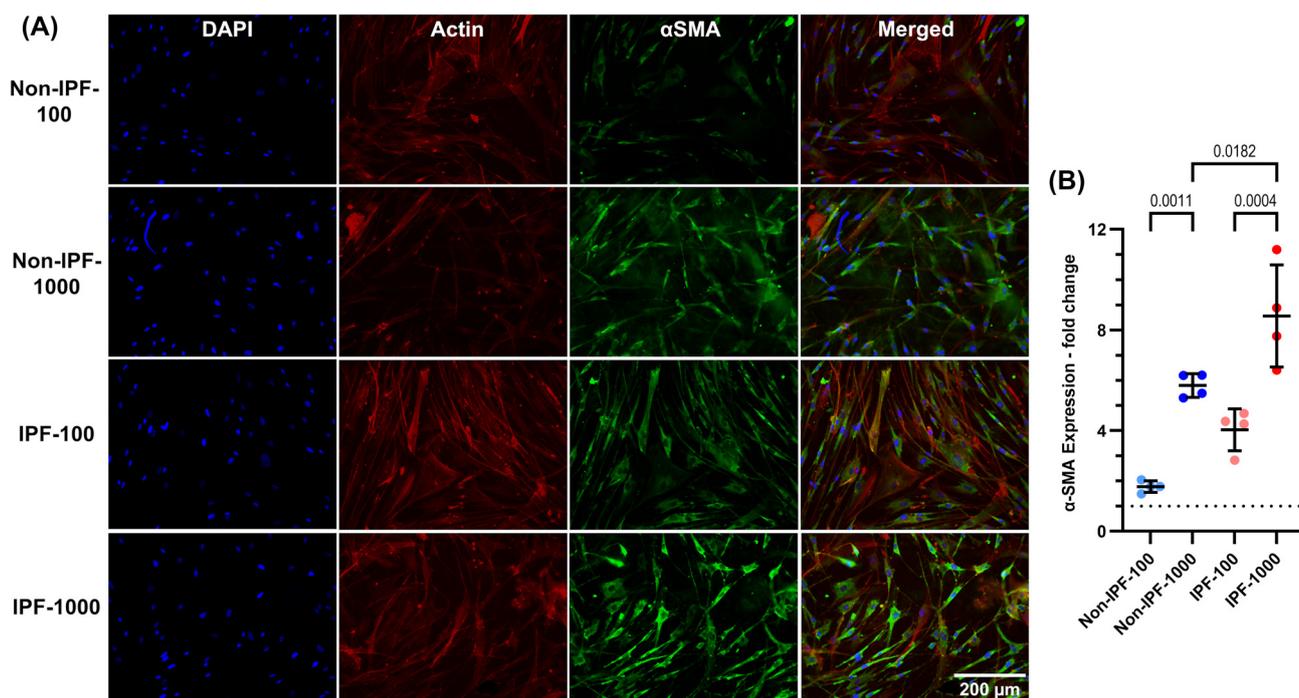

Fig. 5 α-SMA protein expression in HLFs: influence of dECM coating concentration and source. (A) Representative wide-field fluorescence microscopy images depict DAPI-stained nuclei (blue), α-SMA (green), F-actin (red), and merged visualizations. (B) Quantitative analysis of α-SMA expression, measured as the integrated value in the fluorescence signal from the green channel normalized to the number of cells, indicating the fold changes in protein expression compared to TCP indicated as dotted lines in panel B. The dECM coatings, derived from both non-IPF and IPF sources, were found to elevate the expression of α-SMA, indicating that a combination of physcial and biochemical cues plays a role in the fibrotic behavior of HLFs. $n = 4$ experimental replicates with mean values presented with standard deviation. Ordinary one-way ANOVA was used for statistical analysis.
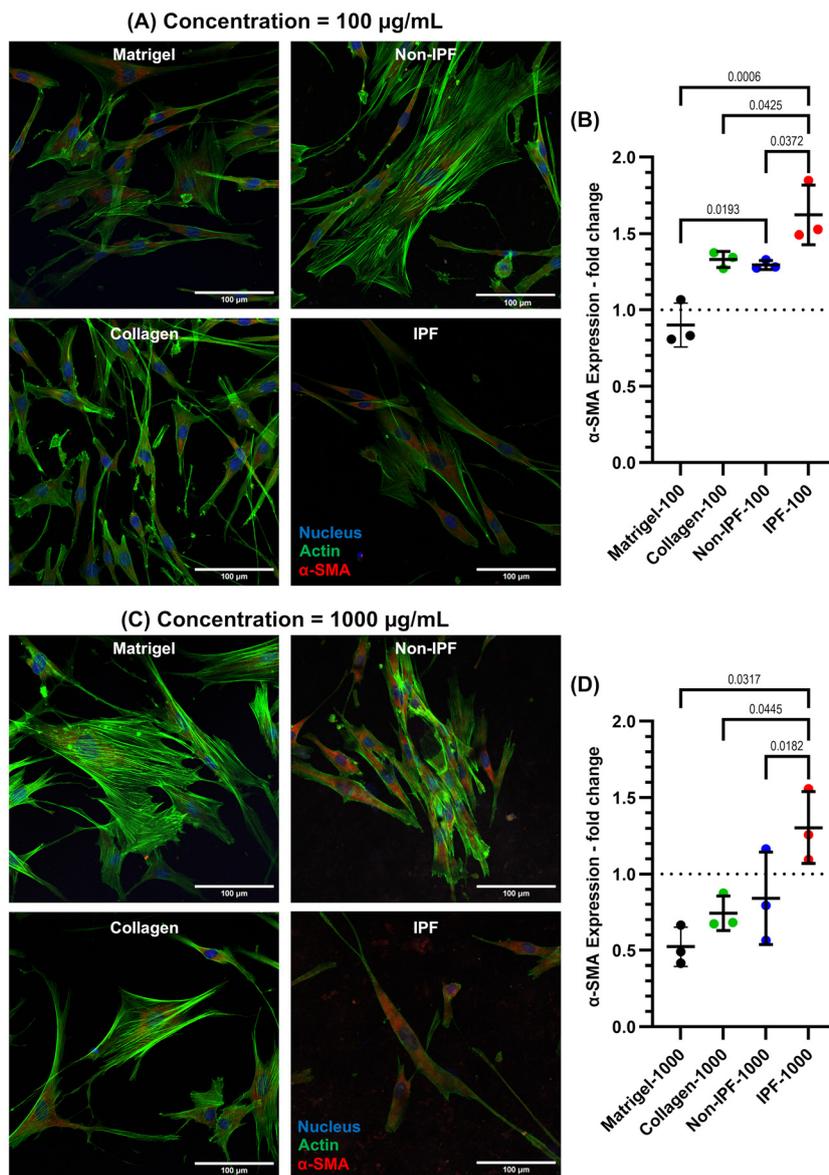
Fig. 6 α-SMA protein expression comparative analysis with HLF cultured on dECM coatings derived from Non-IPF and IPF sources or commercially available collagen-1 and Matrigel. (A) Representative wide-field merged fluorescence microscopy images illustrate DAPI-stained nuclei (blue), α-SMA (red), and F-actin (green) for coatings applied at a concentration of 100 μg ml^{-1}. (B) Quantitative analysis of α-SMA expression across different coatings at a concentration of 100 μg ml^{-1}. The integrated fluorescence signal from the red channel, normalized to cell count and compared to non-coated TCP, indicates that IPF dECM-coated surfaces induce the highest α-SMA protein expression under these conditions. (C) Representative wide-field merged fluorescence microscopy images show DAPI-stained nuclei (blue), α-SMA (red), and F-actin (green) for coatings applied at a concentration of 1000 μg ml^{-1}. (D) Quantitative analysis of α-SMA expression across different coatings at a concentration of 1000 μg ml^{-1}. The integrated fluorescence signal from the red channel, normalized to cell count and compared to non-coated TCP, reveals that IPF dECM-coated surfaces promote the highest α-SMA protein expression under these conditions. Results represent the mean ± standard deviation of three experimental replicates. Statistical analysis was performed using ordinary one-way ANOVA.

composition of IPF dECM rather than the mere presence of an ECM coating.

Effect of dECM coatings on YAP nuclear localization in human lung fibroblasts

We next explored Yes-associated protein (YAP) nuclear localization in HLFs under various conditions, including TCP and surfaces coated with dECM from both non-IPF and IPF lung tissues at concentrations of 100 and 1000 μg ml^{-1} (Fig. 7). YAP analysis was performed at low (5000 cells per cm^2) and high cell densities (20 000 cells per cm^2 – Fig. S5 in the ESI†). A low cell density was chosen to minimize cell-to-cell interaction that might impact YAP activity. YAP was specifically selected for this analysis due to its sensitivity to mechanical cues in the cellular microenvironment and its relevance as a mechanotransduction biomarker.[35] Among all conditions, cells seeded
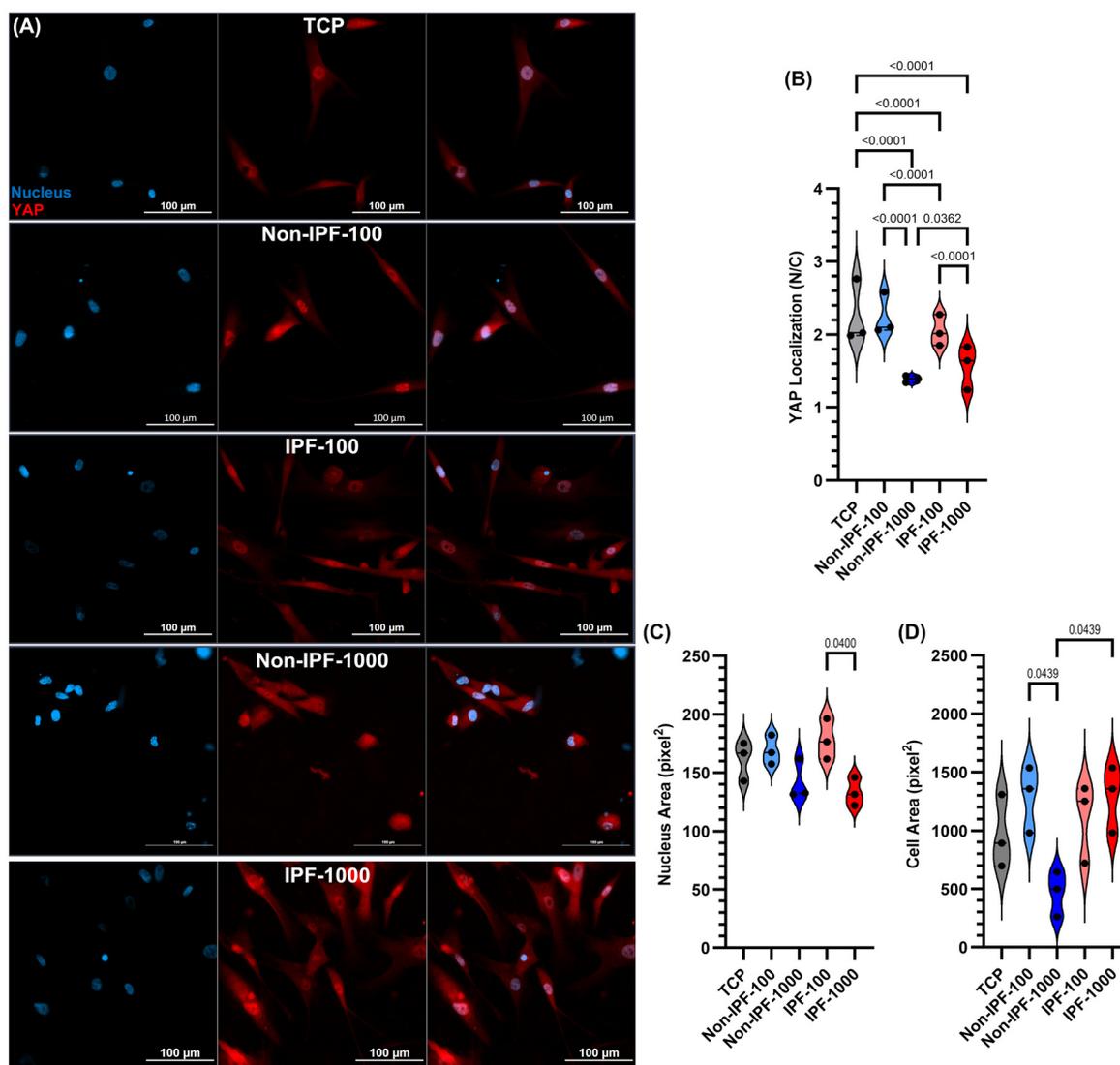
Fig. 7 YAP localization variability in HLFs on dECM coated surfaces: influence of concentration and source at a low cell density of 5000 cells per cm^2. (A) Representative wide-field fluorescent microscopy images showcasing DAPI-stained nuclei (blue) and YAP (red). (B) Quantitative analysis of YAP localization (N = nucleus, C = cytoplasm), measured as the mean gray value in the red channel, illustrating the adjustments in YAP distribution across different dECM coatings and concentrations. (C) Nucleus and (D) cell area analysis. Data are single cell analysis and collected from three indviual donors. Statistical analysis was performed using ordinary one-way ANOVA.

on non-IPF-1000 dECM and IPF-1000 dECM coatings demonstrated the lowest YAP nuclear localization (Fig. 7A and B) compared to other conditions. In contrast, other dECM-coated surfaces led to higher or similar YAP nuclear localization compared to cells seeded on TCP. Moreover, nucleus area and cell area of HLFs cultured on these coatings and the low cell density were analyzed as presented in Fig. 7C and D. These data suggested that cells on non-IPF-1000 experienced different physical cues by becoming smaller compared to cells grown on other coatings and TCP. The data emphasizes the effects that dECM coatings have on cell behavior, particularly through mechanical signaling pathways such as those mediated by YAP and contributes to our understanding of how surface modifications can influence cell mechanics and signaling.

Gene expression profiling of HLFs in response to dECM coating

We next performed select gene expression profiling of HLFs in response to different dECM coatings derived from non-IPF and IPF lung tissues. The genes selected for analysis were *ACTA2*, *CTGF*, *LOX*, *COL1A1*, and *ITGB8*, which are involved in fibrotic processes (Fig. 8). *ACTA2* represents alpha-smooth muscle actin, a marker of myofibroblast activation; *CTGF* is a mechanotransduction biomarker involved in tissue repair and fibrosis; *LOX* is a contributor to extracellular matrix remodeling; *COL1A1* represents type I collagen, a major ECM component; and *ITGB8* is integrin beta 8, involved in cell–matrix interactions.
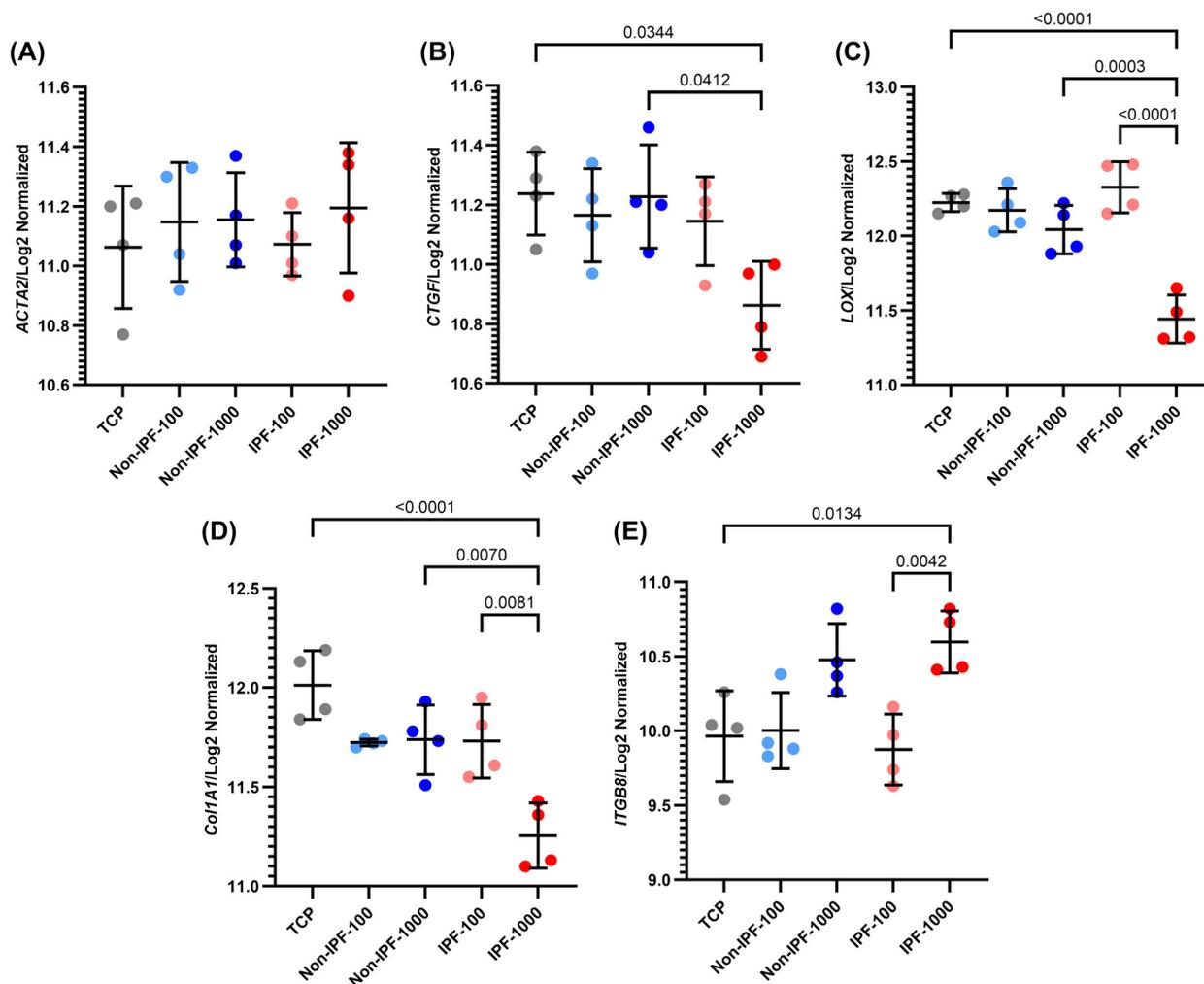
Fig. 8 Gene expression profiling in HLFs on dECM coated surfaces: differential impact of coating source and concentration. (A) *ACTA2*, (B) *CTGF*, (C) *LOX*, (D) *COL1A1*, and (E) *ITGB8* expression quantification across various conditions. These panels represent the expression levels of key fibrotic and cellular interaction genes in response to non-IPF and IPF dECM coatings at different concentrations. Data are means ± SD, *n* = 4.

Our findings indicate that for *ACTA2*, there were no significant differences observed among all groups, although there was a slight, non-significant increase in expression in IPF 1000 μg mL^{-1} dECM coating (Fig. 8A). For *CTGF*, the expression was significantly reduced in the IPF 1000 μg mL^{-1} group compared to the non-IPF 1000 μg mL^{-1} and TCP groups (Fig. 8B). However, there was no significant difference between the IPF 1000 μg mL^{-1} and IPF 100 μg mL^{-1} groups.

LOX expression mirrored the trend observed in *CTGF*, with a significant reduction in IPF 1000 μg mL^{-1} compared to non-IPF 1000 μg mL^{-1} and TCP (Fig. 8C). Moreover, a significant difference was noted between the IPF 1000 μg mL^{-1} and IPF 100 μg mL^{-1} groups, indicating a concentration-dependent response. *COL1A1* expression followed a similar pattern, suggesting alterations in collagen deposition and matrix organization in response to the different dECM coatings (Fig. 8D). Conversely, *ITGB8* showed an opposite trend, with the highest expression levels in the IPF 1000 μg mL^{-1} group,

although not significantly different from the non-IPF 1000 μg mL^{-1} group (Fig. 8E). A significant difference was noted between the IPF 1000 μg mL^{-1} and both the IPF 100 μg mL^{-1} and TCP groups, indicating enhanced cell–matrix interactions or signaling in response to IPF dECM, particularly at higher concentrations.

In this study, we also examined the expression of several integrin subunits in HLFs in response to dECM coatings derived from non-IPF and IPF lung tissues (Fig. 9). Fig. 9A illustrates the expression of integrins specific to cell types and delineates their functional roles in lung fibrosis.[36–39] It categorizes each integrin heterodimer according to its unique recognition and binding capabilities to specific cell adhesion molecules within the ECM or on the cellular surface.[36] The integrin subunits analyzed were *ITGB1*, *ITGA5*, *ITGA8*, *ITGAV*, *ITGB3*, *ITGB5*, and *ITGB8* as depicted in Fig. 9. Our results revealed a distinct downregulation of *ITGB1* in HLFs exposed to the IPF dECM coating at a concentration of 1000 μg ml^{-1},
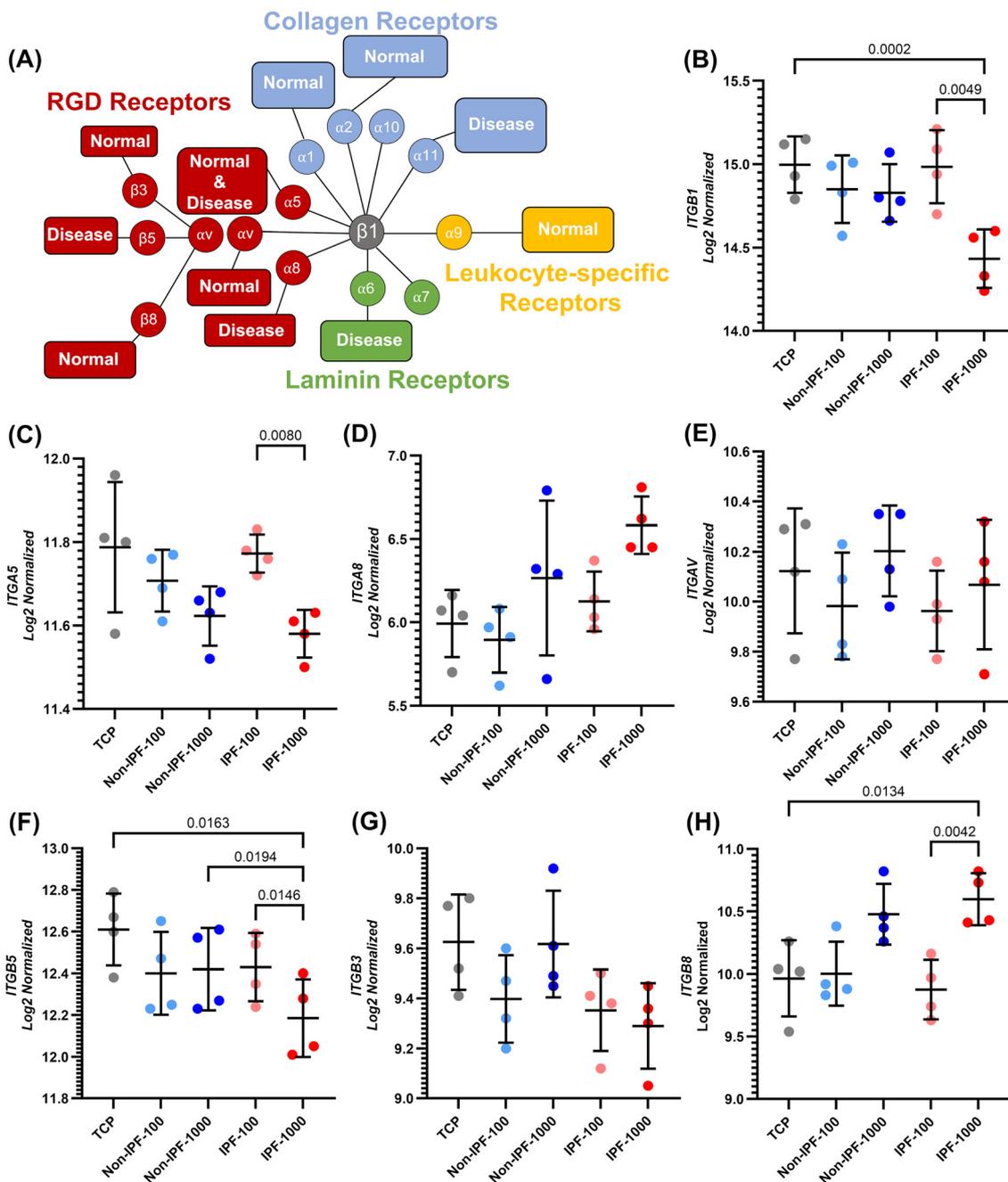
Fig. 9 Integrin-specific gene expression profiling in HLFs on dECM coated surfaces: differential impact of coating source and concentration. (A) Depiction of the various integrin receptor pairs, highlighting their ligand preferences and expression patterns in normal and fibrotic cells. Inspired from Schnittert et al.[36] (B) ITGB1, which can pair with multiple alpha subunits to form different integrin heterodimers, which can bind to a variety of ECM proteins, (C) ITGA5, (D) ITGA8, (E) ITGAV, (F) ITGB5, (G) ITGB3, and (H) ITGB8 expression quantification across various conditions. Data are means $\pm$ SD, $n = 4$.

compared to both the lower concentration of 100 µg ml^{-1} and TCP (Fig. 9B). This trend highlights a specific response to the high-concentration IPF-derived ECM environment. In the analysis of *ITGA5*, *ITGA8*, and *ITGAV*, we observed a differential expression pattern. Notably, *ITGA5* exhibited a significant decrease in expression in the 1000 µg ml^{-1} IPF dECM condition relative to the 100 µg ml^{-1} IPF dECM. The expressions

of *ITGA8* and *ITGAV*, however, did not show similar significant changes under these conditions. Furthermore, within the group comprising ITGB3, *ITGB5*, and *ITGB8*, we observed that *ITGB5* expression was significantly reduced in the 1000 µg ml^{-1} IPF dECM coating compared to both the 100 µg ml^{-1} IPF dECM and the non-IPF dECM at 1000 µg ml^{-1}, as well as TCP. Conversely, *ITGB8* showed an upregulation in expression

under the 1000 µg ml^{-1} IPF dECM condition when compared to both the 100 µg ml^{-1} IPF dECM and TCP.

In our examination of gene expression associated with ECM remodeling, we focused on the influence of dECM coatings sourced from distinct tissue types. We scrutinized the expression patterns of four involved genes—COL1A1, COL3A1, LOX, and FN1—which are known to become dysregulated during wound healing events or in the fibrotic response. For the genes COL1A1 and COL3A1 (Fig. 8D and Fig. S6B – ESI†), which encode the fibrillar collagens type I and type III respectively, a critical component of the ECM, we observed that their expression was significantly lowest in the IPF-1000 condition. This reduction was notable when compared to both the IPF-100 and the non-IPF-1000 groups, as well as the TCP control. Furthermore, the expression of these genes in the IPF-100 group was significantly lower than that in the TCP control, while no significant differences were noted among the other conditions. The gene LOX (Fig. 8C), which encodes lysyl oxidase, an enzyme that cross-links collagens and elastin, also showed the lowest expression in the IPF-1000 group, indicating a diminished capacity for ECM stabilization and repair in this high-concentration IPF-derived ECM environment. Interestingly, LOX expression was highest in the IPF-100 group, although not significantly different from TCP or non-IPF-100, suggesting a nuanced regulatory mechanism at play that may not be linearly dependent on ECM concentration. For the gene FN1 (Fig. S6A – ESI†), responsible for encoding fibronectin, a glycoprotein that binds to integrins and plays a key role in wound healing and fibrosis, the expression was again lowest in the IPF-1000 group. This expression was significantly lower than in the IPF-100 group, but the differences across all conditions were not as pronounced, hinting at a potential threshold effect or a saturation point in the context of fibronectin's role in ECM remodeling.

Discussion

HLFs play a pivotal role in sustaining the structural integrity and functionality of lung tissue by producing and remodeling the ECM, a vital scaffold for cellular support and signaling. The behavior of HLFs, which is influenced by physical and biochemical cues from the microenvironment, is critical in regulating tissue homeostasis, repair mechanisms, and fibrotic processes, particularly relevant in chronic pulmonary conditions like IPF. This work presents an in-depth analysis of the effects of dECM coatings from non-IPF and IPF lung tissues on HLFs biology. Central to our study was a different coating method where the digested dECM solution was allowed to completely dehydrate, ensuring maximal retention of digested dECM components on cell culture surface. We explored the impact of dECM coatings at two concentrations, 100 µg mL^{-1} and 1000 µg mL^{-1}, on cellular morphology, protein expression, and gene regulation. Surface analysis, incorporating AFM, SEM imaging and WCA measurements, confirmed the efficacy of our coating strategy. The morphological assessment of HLFs

indicated significant responses to the dECM coatings, characterized by alterations in cell spreading, shape, and nuclear features. Our findings revealed a notable upregulation of α-SMA on dECM coated surfaces, particularly at the high concentration, indicating a pro-fibrotic response and suggesting that ECM components in the coatings might promote myofibroblast-like behavior. Additionally, the reduced nuclear localization of YAP in cells on dECM surfaces at their highest concentrations pointed to changes in mechanotransduction pathways, likely influenced by the altered mechanical environment or ECM-derived biochemical cues. Gene expression analysis offered deeper insights, showing a significant downregulation of key ECM-related genes in cells exposed to IPF dECM at 1000 µg ml^{-1}. This reflects a complex cellular adaptation to the pathological ECM, mirroring the unique biochemical and mechanical challenges presented by the diseased state.

Our dECM coating strategy takes a non-conventional approach compared to typical ECM protein coatings which usually involves applying a solution of ECM proteins to a surface at a low concentration, followed by the removal of the excess solution to obtain a monolayer of the coating.[29,37–39] We allowed the dECM solution to completely dehydrate, thereby ensuring that a maximal amount of dECM applied remained as a coating. It should be emphasized that this coating strategy is not intended to replace 3D dECM-based hydrogels, which more closely replicate the physiological environment of lung tissue. Instead, it serves as a versatile platform that facilitates the introduction of biochemical cues into the cellular environment. This approach is particularly valuable when numerous variations and variables need to be studied, allowing for extensive experimentation and analysis. This model represents an advancement over simple TCP setups and is less complex than 3D dECM hydrogels. Considering the scarcity and high value of human-based materials, our approach also offers a cost-effective alternative. The stiffness, surface roughness, and thickness of dECM-coated surfaces were measured using AFM (Fig. 2 and Fig. S3, S4 in the ESI†). Coating the surface with either non-IPF or IPF dECM did not alter surface roughness. At a concentration of 1000 µg mL^{-1}, non-IPF-coated surfaces were stiffer than IPF-coated surfaces, though both were significantly softer than TCP.

In understanding cellular and nuclear responses to variations in substrate stiffness, biochemical cues, and surface topography, the measured parameters of cell area, nucleus area, cell eccentricity, and nucleus eccentricity provide critical insights (Fig. 3). Typically, cells spread more extensively and exhibit a larger cell area on stiffer substrates due to enhanced focal adhesion formation and increased cytoskeletal tension, which allow for more extensive cell spreading.[40] Conversely, on softer substrates or those with complex topographies, cells may exhibit a smaller spreading area due to reduced mechanical resistance and altered adhesion dynamics.[24,40] The nucleus area is also influenced by substrate stiffness and biochemical cues, as the nucleus is mechanically integrated with the cytoskeleton.[41,42] Generally, on stiffer substrates, cells not only spread more but may also exert more force on their nuclei,

potentially leading to changes in nuclear area. However, the relationship between substrate stiffness and nuclear area is not as straightforward as with cell area, as it also depends on the nuclear-cytoskeletal coupling and the specific biochemical signals mediated by the ECM. Lovett *et al.* indicated that on thinner gels, the nuclear height of NIH 3T3 fibroblasts did not vary significantly with changes in substrate stiffness, implying that cells may sense the rigidity of the support beneath the gel, whereas on thicker gels, the nuclear height noticeably decreased with increasing substrate stiffness, reflecting the nucleus's responsiveness to the rigidity of the surrounding environment.[41] Our results demonstrated that for TCP and non-IPF dECM coated surfaces with a concentration of 100 μg mL^{-1}, there was no discernible difference in nucleus area. However, for cells cultured on non-IPF dECM coated surfaces with a concentration of 1000 μg mL^{-1} or IPF dECM coated surfaces, there was a modest increase in nucleus area compared to TCP. Given other studies findings that nucleus area tends to enlarge with increased substrate stiffness on sufficiently thick substrates (over 20 μm), the observed increase in nucleus area is likely not arising from an increase in stiffness over TCP but rather attributable to the alterations in surface topography resulting from the deposition of dECM or changes in chemical composition of coating on the surface. Another study showed that nuclei situated on grooved substrates exhibited an increase in area, especially when aligned with the substrate's grooves, in contrast to nuclei on flat substrates.[43] It is plausible that the formation of fiber-like structures on surfaces coated with 1000 μg mL^{-1} dECM could mimic the topographical effects seen with grooved substrates, resulting in a subtle increase in nuclear area similar to the elevation observed in cells interacting with grooved surfaces, compared to those on other substrate conditions. Surface features like ridges, grooves, or fibers inherent in the ECM can guide the alignment of cytoskeletal filaments, leading to directed changes in nuclear shape and orientation, subsequently affecting cellular processes such as migration and polarity.[44]

The addition of ECM proteins, such as collagen, fibronectin, integrins, laminin, and others, has been widely employed in various studies to enhance cell attachment and proliferation.[45–47] These ECM components mimic the natural microenvironment of cells, providing not only structural support but also critical biochemical signals that guide cell adhesion, spreading, and subsequent proliferation. In our study, the application of non-IPF dECM coatings, which are rich in various ECM proteins, demonstrated a similar pattern of improved cell adhesion and proliferation (Fig. 4). The non-IPF dECM coatings provided a biomimetic surface, allowing cells to interact with a complex mixture of proteins akin to their native environment. However, when we introduced coatings derived from IPF lung tissues, a different trend emerged (Fig. 4). The IPF dECM coatings led to a reduction in cell proliferation compared to both the non-IPF dECM coatings. In disease conditions such as IPF, the ECM composition is altered; it often becomes stiffer and exhibits abnormal levels of certain proteins, which can disrupt normal cell

behavior.[28,48–50] Mass spectrometry analyses of fibrotic decellularized scaffolds revealed significant ECM remodeling compared to healthy lung tissue. There was an increase exceeding 150% in the expression of several collagen types, including Types I, II, V, VI, VIII, and XVI, which are key components associated with fibrosis and matrix stiffness.[50] Conversely, collagen types IV and XXI, critical for maintaining the basement membrane's structural integrity, exhibited a reduction of approximately 70% in fibrotic scaffolds.[51] Additionally, glycoproteins such as vitronectin and fibulin-2 were significantly upregulated in fibrotic tissues, contributing to ECM rigidity and impaired cellular function. Other glycoproteins, including periostin and biglycan, showed substantial alterations, correlating with increased profibrotic signaling and fibroblast activation.[52] Laminin subunits α3, β2, γ1, and nidogen-1, essential components of the basement membrane, underwent marked reductions, contributing to disrupted epithelial–mesenchymal interactions and alveolar instability.[51,52] In fibrotic lungs, glycosaminoglycan (GAG) composition was also significantly altered, with increased deposition of hyaluronic acid and chondroitin sulfate and a reduction in heparan sulfate. This change in GAG composition further promotes aberrant tissue remodeling and impacts growth factor signaling.[52] Proteomic studies identified novel ECM proteins, such as collagen XXVIII and emilin-2, within the provisional repair matrix in fibrotic regions, highlighting the dynamic changes occurring during fibrogenesis.[51] Together, these findings illustrate a profound reorganization of ECM components in IPF, emphasizing increased matrix deposition, altered glycoprotein expression, and the loss of basement membrane integrity, which collectively disrupt normal lung architecture and promote progressive fibrosis.[50–56] The altered biochemical composition of the IPF dECM might have provided signals that are less conducive to cell proliferation or even inhibitory compared to the non-IPF dECM. Furthermore, the reduced proliferation observed in cells on IPF dECM coatings suggests that not all ECM coatings are equally beneficial and that the source of the ECM, reflecting the health or disease state of the tissue, is a critical factor in determining the coating's impact on cell behavior. The reduction in cell proliferation on IPF dECM coatings was more pronounced at the highest concentration, where cell proliferation rates on IPF dECM coatings were similar to those on uncoated TCP. At the lower concentration, while cell proliferation on IPF dECM was still higher compared to TCP, it was reduced relative to non-IPF dECM coatings (Fig. 4).

In our study, we investigated α-SMA expression in HLFs in response to dECM coatings from both non-IPF and IPF lung tissues, focusing on the source and concentration of dECM as key variables. Our results showed increased α-SMA expression in cells on both non-IPF and IPF dECM coatings, especially at the highest concentration of IPF dECM coating compared to uncoated TCP. This was notable especially on the stiffer TCP substrate, which typically induces more fibrotic behavior,[9] suggesting that the dECM coatings provided additional cues influencing α-SMA expression beyond the usual stiffness-mediated effects. Furthermore, the concentration-dependent

increase in α-SMA expression indicates that the amount and arrangement of ECM material on the surface are significant in modulating cellular responses, possibly by changing the local mechanical environment or presenting different biochemical cues. We included two additional types of ECM coatings in our study: collagen, representing a single, homogeneous ECM component, and Matrigel, representing a more complex, heterogeneous ECM substrate. When comparing IPF dECM coatings at both 100 and 1000 μg mL^{-1} concentrations to collagen- and Matrigel-coated surfaces, we observed an increase in α-SMA expression in HLFs grown on IPF dECM. This finding suggests that the inherently fibrotic nature of IPF dECM coatings not only supports a myofibroblast phenotype but also more closely mimics the pathological conditions of fibrotic tissue, thereby providing a physiologically relevant model system for investigating IPF-related fibroblast activation and disease progression. The α-SMA expression of cells seeded on dECM coatings at high and low cell densities, as shown in Fig. 5 and 6, likely reflects the impact of variations in experimental conditions between the two setups. Specifically, the experiments used cells from different donors and passages, which can influence their baseline α-SMA expression. Additionally, in Fig. 5, cells were seeded at high density and reached confluency, a condition known to enhance α-SMA expression due to increased cell–cell interactions.[57,58] In contrast, in Fig. 6, low-density seeding was used to minimize cell–cell interactions and focus on the effects of the dECM coatings. These differences in cell density, donor variability, and passage number likely contributed to the observed variations in the fold change values for α-SMA expression. The results suggest that the specific composition, structure, and concentration of ECM coatings can significantly influence pathways regulating α-SMA expression and can be harnessed to guide cell behavior.

YAP nuclear localization is influenced by the stiffness of the ECM or the substrate and the cell geometric shape.[35,59,60] Typically, a stiffer ECM encourages cells to spread more, promoting YAP nuclear localization and signaling for cellular proliferation and tissue growth.[61] On the other hand, softer matrices or confined spaces lead to a greater likelihood of YAP staying in the cytoplasm, thus dampening growth signals.[61] This mechanical sensitivity makes YAP a fundamental intermediary in translating cues from the external environment into cellular responses. In our experiments, we observed reduced YAP localization in cells grown on both non-IPF-1000 and IPF-1000 dECM-coated surfaces compared to other conditions (Fig. 7). AFM analysis revealed that high concentrations of dECM coatings produced thicker (>1 micron), softer surfaces. In contrast, the non-IPF-100 and IPF-100 dECM coatings, which formed submicron-scale thickness, exhibited levels of YAP nuclear localization comparable to those observed on TCP. In addition, we examined YAP localization at a cell density of 20 000 cells per cm^2 that promotes confluence and enhances cell-to-cell interactions (Fig. S5 in the ESI†). Under these conditions, YAP nuclear localization was generally minimal, with a modest increase noted for non-IPF-1000

dECM coatings. These observations imply that while the physical modifications induced by the dECM are sufficient to modulate YAP signaling, reducing direct cell-to-cell interactions may be necessary to fully discern the matrix's influence on this process.

When interpreting both α-SMA expression and YAP localization together, it becomes apparent that cells are integrating a complex set of signals from the dECM coatings. The upregulation of α-SMA might be driven more by the specific biochemical composition of the dECM, including fibrosis-associated proteins, which could stimulate myofibroblast differentiation irrespective of the substrate's mechanical properties. In contrast, the reduction in YAP nuclear localization suggests that cells are sensing an altered mechanical environment, perhaps due to changes in topography introduced by the dECM coatings. Among the two, YAP localization seems more directly related to the immediate mechanical or physcial environment, making it a sensitive indicator of how cells perceive changes in substrate stiffness and topography. However, the expression of α-SMA provides critical information about the longer-term phenotypic adaptation of cells, particularly in the context of fibrosis and tissue repair. Both markers are relevant, but the prominence of each in our study might depend on the specific aspect of cell behavior or adaptation we aimed to understand.

The gene expression data from our study, particularly the downregulation of CTGF, LOX, and COL1A1 in IPF dECM coatings at 1000 μg ml^{-1}, provides a nuanced view of how HLFs respond to varying dECM conditions.[62,63] Our study revealed that contrary to expectations of gene upregulation in response to a fibrotic ECM, there was a notable downregulation, potentially due to several factors.[48] The biochemical environment of IPF-derived dECM, differing significantly from normal tissue, might lack stimulatory factors or present inhibitory signals, leading to suppressed expression of ECM-related genes.[55,64] This reflects the pathological changes in IPF tissues, potentially triggering a regulatory response to downregulate genes involved in ECM production and crosslinking. Additionally, cells might engage in negative feedback mechanisms to limit excessive ECM deposition in fibrotic conditions. Furthermore, the interaction with diseased ECM could induce cellular stress or alter signaling pathways, resulting in reduced expression of genes typically upregulated in fibrosis. This suggests a complex cellular adaptation or impaired function due to disease. The disparity between α-SMA protein expression and ACTA2 gene expression indicates that gene expression analysis can be influenced by timing and cellular state, with transcription and translation processes responding differently to environmental changes. The gene expression patterns confirm the multifaceted cellular response to ECM coatings, reflecting both biochemical composition and mechanical properties of the substrate. The significant impact of ECM source (non-IPF vs. IPF) and concentration on cell behavior is highlighted, with the pathological state of IPF dECM inducing distinct gene expression changes.

In addition, we explored the differential expression of various integrin subunits in HLFs in response to dECM coat-

ings derived from non-IPF and IPF tissues. A notable observation in our study is the downregulation of *ITGB1* in the IPF-1000 condition compared to both IPF-100 and TCP. *ITGB1* plays a pivotal role in mediating cell adhesion and signaling through interactions with various ECM proteins. Its downregulation in the context of high-concentration IPF dECM suggests an altered capacity for HLFs to interact with the ECM, potentially leading to changes in cellular behaviors such as migration and mechanotransduction. This could reflect an adaptive response to the altered ECM composition in IPF, indicating a shift in cell–ECM interaction dynamics that may contribute to the pathophysiology of the disease. These integrins (*ITGA5*, *ITGA8*, and *ITGAV*) primarily interact with RGD motifs found in proteins like fibronectin. Among these, *ITGA5* was specifically downregulated in the IPF-1000 condition compared to IPF-100. This could suggest a selective alteration in the cell's ability to bind fibronectin, a key component of the ECM. Such a change in *ITGA5* expression could impact crucial cellular processes, including adhesion and migration, and highlights the specificity of cellular responses to changes in the ECM, especially in fibrotic conditions like IPF. For *ITGB3*, *ITGB5*, and *ITGB8*, we observed that *ITGB5* was significantly downregulated in IPF-1000 compared to IPF-100, non-IPF-1000, and TCP, while *ITGB8* showed upregulation in the IPF-1000 condition. The downregulation of *ITGB5*, known for its role in angiogenesis and cell migration, suggests a diminished interaction with ECM components like vitronectin in the high-concentration IPF dECM. Conversely, the upregulation of *ITGB8*, which is involved in activating latent growth factors, indicates a potential increase in the activation of pathways like TGF-β signaling, known to contribute to fibrotic processes.[65] The findings indicated that non-IPF dECM coatings promote better cell adhesion and proliferation compared to uncoated TCP, with no significant difference between the two concentrations of non-IPF dECM (100 μg ml^{-1} and 1000 μg ml^{-1}). This enhanced cellular response correlates with the integrin expression patterns where certain integrins like *ITGB1* and *ITGA5* did not show drastic downregulation, maintaining the cells' capacity for ECM interaction and signaling. The relatively stable expression of these integrins could contribute to the observed improvements in cell adhesion and proliferation on non-IPF dECM coatings. In stark contrast, cells seeded on IPF dECM coatings exhibited reduced proliferation rates, especially at the higher concentration of 1000 μg ml^{-1}. This aligns with the observed downregulation of *ITGB1* and *ITGA5* under the IPF-1000 condition, suggesting a diminished integrin-mediated interaction with the ECM. The significant reduction in cell proliferation on 1000 μg ml^{-1} IPF dECM, to levels comparable with TCP, emphasizes the impact of fibrotic ECM on cellular functions. The altered integrin expression in response to the IPF dECM, particularly at higher concentrations, reflects a possible mechanistic link between disrupted cell–ECM interactions and reduced cell proliferation. Furthermore, the differences observed between the 100 μg ml^{-1} and 1000 μg ml^{-1} concentrations of IPF dECM coatings imply a concentration-dependent cellular response. This is particularly evident in the

upregulation of *ITGB8* under the IPF-1000 condition, which may indicate an adaptive response or a pathological aspect of the disease progression. Overall, our findings suggest that the source and concentration of dECM—non-IPF *versus* fibrotic diseased tissue—play crucial roles in modulating HLF behavior. The integrin expression changes in response to different dECM environments highlight the complex regulation of cell–ECM interactions. These insights emphasize the importance of considering both biochemical and mechanical cues from the ECM in understanding cell behavior in health and disease. They also underscore the potential for targeting specific integrin–ECM interactions in therapeutic strategies for fibrotic diseases like IPF, where modulation of these interactions could alter disease progression or severity.

In advancing our understanding of cell–ECM interactions, future studies should aim to decouple mechanical/physical from biochemical cues. This could involve using substrates with varied stiffness, ranging from the rigidity of TCP to softer materials. Such diversity in substrate stiffness would allow for a more nuanced understanding of how mechanical properties influence cell behavior independently from the biochemical composition of the ECM. Grasping the distinct and combined effects of mechanical and biochemical cues is vital for designing biomaterials that more faithfully replicate the natural cellular environment that could be used in regenerative medicine applications. Another critical area is considering the temporal dynamics of cellular pathways. For instance, studying the time-sensitive YAP pathway could reveal differing responses during early cell–substrate interactions, where mechanical cues are predominant, compared to later stages dominated by biochemical cues. Time-dependent studies are essential to comprehend the immediate *versus* long-term effects of ECM coatings on cellular behavior and the dynamics of mechanosensitive pathways like YAP. Investigating focal adhesions in future research could also offer significant insights. These structures are crucial in mediating both mechanical and biochemical signals between the cell and its substrate. By examining the formation, composition, and dynamics of focal adhesions, researchers can gain a deeper understanding of how cells interpret and respond to their microenvironment. Additionally, conducting detailed temporal studies of cell adhesion and proliferation from the moment of seeding onto coated surfaces until confluence could elucidate the distinct contributions of these processes. This approach would help to differentiate the roles and timing of adhesion and proliferation, leading to a clearer understanding of their relative impacts on cell growth on different substrates. By addressing these areas, future research can build on our findings to develop a more comprehensive understanding of cell–ECM interactions.

Conclusion

In conclusion, our study provides a comprehensive evaluation of the effects of dECM coatings from non-IPF and IPF

lung tissues on HLF biology. By employing a novel dehydration coating strategy that maximizes the retention of dECM on the surface, we were able to explore the impact of both the biochemical composition and the concentration of the dECM on cellular morphology, protein expression, and gene regulation. The morphological analysis of HLFs revealed that cells respond to the dECM coatings with changes in spreading, shape, and nuclear characteristics, demonstrating the cells' sensitivity to both the physcial properties and the biochemical cues of the ECM. The upregulation of α-SMA on dECM coated surfaces, particularly at the highest concentration, signifies a pro-fibrotic response, suggesting that ECM components in the coatings promote myofibroblast-like behavior. In addition, the dysregulation of nuclear localization of YAP in cells on dECM coatings indicates an alteration in mechanotransduction pathways, likely due to changes in the mechanical/physical environment or the presentation of biochemical signals from the ECM. Our gene expression analysis provided further insights into the cellular response to dECM coatings, highlighting a significant downregulation of several key ECM-related genes in cells exposed to high concentrations of IPF dECM. This suggests a complex regulatory adaptation to the pathological ECM, reflecting the altered biochemical and mechanical cues associated with the diseased state. This study underscores the nuanced nature of cell–ECM interactions and the critical role of both ECM physical properties and biochemical composition in influencing cell biology. The findings highlight the importance of considering the source and concentration of ECM in designing biomaterials and the potential of using dECM coatings to modulate cellular responses for tissue engineering and regenerative medicine applications. Overall, our work emphasizes the potential of dECM-derived coatings as powerful tools for studying cellular responses to the ECM, offering insights into the mechanisms of fibrosis, and providing a platform for developing more effective therapeutic strategies.

Author contributions

Conceptualization: MD, JMM, and JAH, data curation: MD, TG, CFD, JMM, and JAH, formal analysis: MD, TG, CFD, JMM, and JAH, funding acquisition: JAH, investigation: MD, RS, AN, AAT, DGM, CFD, JMM, and JAH, methodology: MD, CFD, JMM, and JAH, project administration: MD, and JAH, resources: MD, AN, AAT, DGM, IOR, MRK, YS, JMM, and JAH, software: MD, supervision: JMM and JAH, validation: MD, AAT, DGM, CFD, JMM, and JAH, visualization: MD, CFD, JMM, and JAH, writing – original draft: MD, CFD, JMM, and JAH, and writing – review & editing: all authors.

Data availability

The data is available upon reasonable request.

All data generated or analyzed during this study are included in this published article. Additional data will be made available upon reasonable request.

Conflicts of interest

The authors declare no conflict of interest.

Acknowledgements

References

1 F. Chua, J. Gauldie and G. J. Laurent, Pulmonary Fibrosis, *Am. J. Respir. Cell Mol. Biol.*, 2005, **33**(1), 9–13.

2 T. Kulkarni, P. O'Reilly, V. B. Antony, A. Gaggar and V. J. Thannickal, Matrix Remodeling in Pulmonary Fibrosis and Emphysema, *Am. J. Respir. Cell Mol. Biol.*, 2016, **54**(6), 751–760.

3 E. R. Fernández Pérez, C. E. Daniels, J. St. Sauver, T. E. Hartman, B. J. Bartholmai, E. S. Yi, *et al.*, Incidence, Prevalence, and Clinical Course of Idiopathic Pulmonary Fibrosis: A Population-Based Study, *Chest*, 2010, **137**(1), 129–137.

4 J. Tashiro, G. A. Rubio, A. H. Limper, K. Williams, S. J. Elliot, I. Ninou, V. Aidinis, A. Tzouvelekis and M. K. Glassberg, Exploring animal models that resemble idiopathic pulmonary fibrosis, *Front. Med.*, 2017, **4**, 118.

5 A. S. Abhilash, B. M. Baker, B. Trappmann, C. S. Chen and V. B. Shenoy, Remodeling of Fibrous Extracellular Matrices by Contractile Cells: Predictions from Discrete Fiber Network Simulations, *Biophys. J.*, 2014, **107**(8), 1829–1840.

6 B. M. Baker, B. Trappmann, W. Y. Wang, M. S. Sakar, I. L. Kim, V. B. Shenoy, *et al.*, Cell-mediated fibre recruitment drives extracellular matrix mechanosensing in engineered fibrillar microenvironments, *Nat. Mater*, 2015, **14**(12), 1262–1268.

7 M. Dabaghi, M. Barreiro Carpio, N. Saraei, J. M. Moran-Mirabal, M. R. Kolb and J. A. Hirota, A roadmap for developing and engineering in vitro pulmonary fibrosis models, *Biophys. Rev.*, 2023, **4**(2), 021302.

8 Y. Zhou, J. C. Horowitz, A. Naba, N. Ambalavanan, K. Atabai, J. Balestrini, *et al.*, Extracellular matrix in lung development, homeostasis and disease, *Matrix Biol.*, 2018, **73**, 77–104.

9 J. L. Balestrini, S. Chaudhry, V. Sarrazy, A. Koehler and B. Hinz, The mechanical memory of lung myofibroblasts, *Integr. Biol.*, 2012, **4**(4), 410.

10 B. Hinz, Mechanical Aspects of Lung Fibrosis, *Proc. Am. Thorac. Soc.*, 2012, **9**(3), 137–147.

11 M. D. Davidson, J. A. Burdick and R. G. Wells, Engineered Biomaterial Platforms to Study Fibrosis, *Adv. Healthcare Mater.*, 2020, **9**(8), 1901682.

12 S. Makaremi, H. Luu, J. P. Boyle, Y. Zhu, C. Cerson, D. M. E. Bowdish, *et al.*, The Topography of Silica Films Modulates Primary Macrophage Morphology and Function, *Adv. Mater. Interfaces*, 2019, **6**(21), 1900677.

13 M. Guvendiren, M. Perepelyuk, R. G. Wells and J. A. Burdick, Hydrogels with differential and patterned mechanics to study stiffness-mediated myofibroblastic differentiation of hepatic stellate cells, *J. Mech. Behav. Biomed. Mater.*, 2014, **38**, 198–208.

14 H. Lv, L. Li, M. Sun, Y. Zhang, L. Chen, Y. Rong, *et al.*, Mechanism of regulation of stem cell differentiation by matrix stiffness, *Stem Cell Res. Ther.*, 2015, **6**(1), 103.

15 F. M. Watt and W. T. S. Huck, Role of the extracellular matrix in regulating stem cell fate, *Nat. Rev. Mol. Cell Biol.*, 2013, **14**(8), 467–473.

16 K. C. Clause and T. H. Barker, Extracellular matrix signaling in morphogenesis and repair, *Curr. Opin. Biotechnol.*, 2013, **24**(5), 830–833.

17 K. H. Nakayama, L. Hou and N. F. Huang, Role of Extracellular Matrix Signaling Cues in Modulating Cell Fate Commitment for Cardiovascular Tissue Engineering, *Adv. Healthcare Mater.*, 2014, **3**(5), 628–641.

18 J. H. Park, S. B. Jo, J. H. Lee, H. H. Lee, J. C. Knowles and H. W. Kim, Materials and extracellular matrix rigidity highlighted in tissue damages and diseases: Implication for biomaterials design and therapeutic targets, *Bioact. Mater.*, 2023, **20**, 381–403.

19 M. S. Ting, J. Travas-Sejdic and J. Malmström, Modulation of hydrogel stiffness by external stimuli: soft materials for mechanotransduction studies, *J. Mater. Chem. B*, 2021, **9**(37), 7578–7596.

20 U. Blache, E. M. Ford, B. Ha, L. Rijns, O. Chaudhuri, P. Y. W. Dankers, *et al.*, Engineered hydrogels for mechanobiology, *Nat. Rev. Methods Primers*, 2022, **2**(1), 1–22.

21 M. Dabaghi, M. B. Carpio, J. M. Moran-Mirabal and J. A. Hirota, 3D (bio)printing of lungs: past, present, and future, *Eur. Respir. J.*, 2023, **61**(1), 2200417.

22 A. Marinković, F. Liu and D. J. Tschumperlin, Matrices of Physiologic Stiffness Potently Inactivate Idiopathic Pulmonary Fibrosis Fibroblasts, *Am. J. Respir. Cell Mol. Biol.*, 2013, **48**(4), 422–430.

23 K. E. C. Blokland, M. Nizamoglu, H. Habibie, T. Borghuis, M. Schuliga, B. N. Melgert, *et al.*, Substrate stiffness engineered to replicate disease conditions influence senescence and fibrotic responses in primary lung fibroblasts, *Front. Pharmacol.*, 2022, **13**, 989169.

24 S. Asano, S. Ito, K. Takahashi, K. Furuya, M. Kondo, M. Sokabe, *et al.*, Matrix stiffness regulates migration of human lung fibroblasts, *Physiol. Rep.*, 2017, **5**(9), e13281.

25 M. Brown, J. Li, C. Moraes, M. Tabrizian and N. Y. K. Li-Jessen, Decellularized extracellular matrix: New promising and challenging biomaterials for regenerative medicine, *Biomaterials*, 2022, **289**, 121786.

26 M. Dabaghi, N. Saraei, M. B. Carpio, V. Nanduri, J. Ungureanu, M. Babi, *et al.*, A Robust Protocol for Decellularized Human Lung Bioink Generation Amenable to 2D and 3D Lung Cell Culture, *Cells*, 2021, **10**(6), 1538.

27 M. Nizamoglu, R. H. J. de Hilster, F. Zhao, P. K. Sharma, T. Borghuis, M. C. Harmsen, *et al.*, An in vitro model of fibrosis using crosslinked native extracellular matrix-derived hydrogels to modulate biomechanics without changing composition, *Acta Biomater.*, 2022, **147**, 50–62.

28 J.F Davila, D.W Moore, J. Kim, J.A Khan, A.K Singh, M. Lemma, *et al.*, Pulmonary Matrix Derived Hydrogels from Patients with Idiopathic Pulmonary Fibrosis Induce a Proinflammatory State in Lung Fibroblasts In Vitro [Internet]. bioRxiv; 2023. 2023.05.03.539323. Available from:**https://www.biorxiv.org/content/10.1101/2023.05.03.539323v2** [cited 2023 Dec 27].

29 S. E. Gilpin, Q. Li, D. Evangelista-Leite, X. Ren, D. P. Reinhardt, B. L. Frey, *et al.*, Fibrillin-2 and Tenascin-C bridge the age gap in lung epithelial regeneration, *Biomaterials*, 2017, **140**, 212–219.

30 J. L. Hutter and J. Bechhoefer, Calibration of atomic–force microscope tips, *Rev. Sci. Instrum.*, 1993, **64**(7), 1868–1873.

31 C. A. Schneider, W. S. Rasband and K. W. Eliceiri, NIH Image to ImageJ: 25 years of image analysis, *Nat. Methods*, 2012, **9**(7), 671–675.

32 J. Schindelin, I. Arganda-Carreras, E. Frise, V. Kaynig, M. Longair, T. Pietzsch, *et al.*, Fiji: an open-source platform for biological-image analysis, *Nat. Methods*, 2012, **9**(7), 676–682.

33 D. R. Stirling, M. J. Swain-Bowden, A. M. Lucas, A. E. Carpenter, B. A. Cimini and A. Goodman, CellProfiler 4: improvements in speed, utility and usability, *BMC Bioinf.*, 2021, **22**(1), 433.

34 E. A. Ayaub, K. Tandon, M. Padwal, J. Imani, H. Patel, A. Dubey, *et al.*, IL-6 mediates ER expansion during hyperpolarization of alternatively activated macrophages, *Immunol. Cell Biol.*, 2019, **97**(2), 203–217.

35 S. Piccolo, S. Dupont and M. Cordenonsi, The Biology of YAP/TAZ: Hippo Signaling and Beyond, *Physiol. Rev.*, 2014, **94**(4), 1287–1312.

36 J. Schnittert, R. Bansal, G. Storm and J. Prakash, Integrins in wound healing, fibrosis and tumor stroma: High potential targets for therapeutics and drug delivery, *Adv. Drug Delivery Rev.*, 2018, **129**, 37–53.

37 B. M. Young, K. Shankar, C. K. Tho, A. R. Pellegrino and R. L. Heise, Laminin-driven Epac/Rap1 regulation of epithelial barriers on decellularized matrix, *Acta Biomater.*, 2019, **100**, 223–234.

38 J. Fu, Y. J. Chuah, J. Liu, S. Y. Tan and D. A. Wang, Respective Effects of Gelatin-Coated Polydimethylsiloxane

(PDMS) Substrates on Self-renewal and Cardiac Differentiation of Induced Pluripotent Stem Cells (iPSCs), *ACS Biomater. Sci. Eng.*, 2018, **4**(12), 4321–4330.

39 M. Sgarioto, P. Vigneron, J. Patterson, F. Malherbe, M. D. Nagel and C. Egles, Collagen type I together with fibronectin provide a better support for endothelialization, *C. R. Biol.*, 2012, **335**(8), 520–528.

40 T. Yeung, P. C. Georges, L. A. Flanagan, B. Marg, M. Ortiz, M. Funaki, *et al.*, Effects of substrate stiffness on cell morphology, cytoskeletal structure, and adhesion, *Cell Motil. Cytoskeleton*, 2005, **60**(1), 24–34.

41 D. B. Lovett, N. Shekhar, J. A. Nickerson, K. J. Roux and T. P. Lele, Modulation of Nuclear Shape by Substrate Rigidity, *Cell. Mol. Bioeng.*, 2013, **6**(2), 230–238.

42 M. Crisp, Q. Liu, K. Roux, J. B. Rattner, C. Shanahan, B. Burke, *et al.*, Coupling of the nucleus and cytoplasm: Role of the LINC complex, *J. Cell Biol.*, 2005, **172**(1), 41–53.

43 M. J. Dalby, M. O. Riehle, S. J. Yarwood, C. D. W. Wilkinson and A. S. G. Curtis, Nucleus alignment and cell signaling in fibroblasts: response to a micro-grooved topography, *Exp. Cell Res.*, 2003, **284**(2), 272–280.

44 L. Ge, L. Yang, R. Bron, J. K. Burgess and P. van Rijn, Topography-Mediated Fibroblast Cell Migration Is Influenced by Direction, Wavelength, and Amplitude, *ACS Appl. Bio Mater.*, 2020, **3**(4), 2104–2116.

45 J. S. Lee, J. Shin, H. M. Park, Y. G. Kim, B. G. Kim, J. W. Oh, *et al.*, Liver Extracellular Matrix Providing Dual Functions of Two-Dimensional Substrate Coating and Three-Dimensional Injectable Hydrogel Platform for Liver Tissue Engineering, *Biomacromolecules*, 2014, **15**(1), 206–218.

46 S. Kuddannaya, Y. J. Chuah, M. H. A. Lee, N. V. Menon, Y. Kang and Y. Zhang, Surface Chemical Modification of Poly(dimethylsiloxane) for the Enhanced Adhesion and Proliferation of Mesenchymal Stem Cells, *ACS Appl. Mater. Interfaces*, 2013, **5**(19), 9777–9784.

47 D. Kim, S. Eom, S. M. Park, H. Hong and D. S. Kim, A collagen gel-coated, aligned nanofiber membrane for enhanced endothelial barrier function, *Sci. Rep.*, 2019, **9**(1), 14915.

48 A. J. Booth, R. Hadley, A. M. Cornett, A. A. Dreffs, S. A. Matthes, J. L. Tsui, *et al.*, Acellular Normal and Fibrotic Human Lung Matrices as a Culture System for In Vitro Investigation, *Am. J. Respir. Crit. Care Med.*, 2012, **186**(9), 866–876.

49 A. Strikoudis, A. Cieślak, L. Loffredo, Y. W. Chen, N. Patel, A. Saqi, *et al.*, Modeling of Fibrotic Lung Disease Using 3D Organoids Derived from Human Pluripotent Stem Cells, *Cell Rep.*, 2019, **27**(12), 3709–3723.e5.

50 I. Germanguz, E. Aranda, J. C. Xiong, N. Kissel, A. Nichols, E. Gadee and J. D. O'Neill, Fibrotic human lung extracellular matrix as a disease-specific substrate for 3D in-vitro models of pulmonary fibrosis, *bioRxiv*, 2019, 833913.

51 H. B. Schiller, I. E. Fernandez, G. Burgstaller, C. Schaab, R. A. Scheltema, T. Schwarzmayr, *et al.*, Time– and compartment–resolved proteome profiling of the extracellular niche in lung injury and repair, *Mol. Syst. Biol.*, 2015, **11**(7), 819.

52 X. Zhu, Y. Yang, S. Mao, Q. Liu, Y. Li, Y. Yang, M. Gao, J. Bao, W. Li and Y. Li, Lung dECM matrikine-based hydrogel reverses bleomycin-induced pulmonary fibrosis by suppressing M2 macrophage polarization, *Biofabrication*, 2024, **17**(1), 015037.

53 Y. Tian, H. Li, Y. Gao, C. Liu, T. Qiu, H. Wu, *et al.*, Quantitative proteomic characterization of lung tissue in idiopathic pulmonary fibrosis, *Clin. Proteomics*, 2019, **16**(1), 6.

54 X. L. Wan, Z. L. Zhou, P. Wang, X. M. Zhou, M. Y. Xie, J. Mei, *et al.*, Small molecule proteomics quantifies differences between normal and fibrotic pulmonary extracellular matrices, *Chin. Med. J.*, 2020, **133**(10), 1192.

55 E. Hoffman, Y. Song, F. Zhang, L. Asarian, I. Downs, B. Young, *et al.*, Regional and disease-specific glycosaminoglycan composition and function in decellularized human lung extracellular matrix, *Acta Biomater.*, 2023, **168**, 388–399.

56 D. Evangelista-Leite, A. C. O. Carreira, M. Y. Nishiyama, S. E. Gilpin and M. A. Miglino, The molecular mechanisms of extracellular matrix-derived hydrogel therapy in idiopathic pulmonary fibrosis models, *Biomaterials*, 2023, **302**, 122338.

57 D. O. Son, R. Benitez, L. Diao and B. Hinz, How to Keep Myofibroblasts under Control: Culture of Mouse Skin Fibroblasts on Soft Substrates, *J. Invest. Dermatol.*, 2024, **144**(9), 1923–1934.

58 M. T. Doolin, I. M. Smith and K. M. Stroka, Fibroblast to myofibroblast transition is enhanced by increased cell density, *Mol. Biol. Cell*, 2022, **32**(22), ar41.

59 A. Das, R. S. Fischer, D. Pan and C. M. Waterman, YAP Nuclear Localization in the Absence of Cell-Cell Contact Is Mediated by a Filamentous Actin-dependent, Myosin II- and Phospho-YAP-independent Pathway during Extracellular Matrix Mechanosensing, *J. Biol. Chem.*, 2016, **291**(12), 6096–6110.

60 B. Cheng, M. Li, W. Wan, H. Guo, G. M. Genin, M. Lin, *et al.*, Predicting YAP/TAZ nuclear translocation in response to ECM mechanosensing, *Biophys. J.*, 2023, **122**(1), 43–53.

61 G. Brusatin, T. Panciera, A. Gandin, A. Citron and S. Piccolo, Biomaterials and engineered microenvironments to control YAP/TAZ-dependent cell behaviour, *Nat. Mater.*, 2018, **17**(12), 1063–1075.

62 A. Hanmandlu, L. Zhu, T. C. J. Mertens, S. Collum, W. Bi, F. Xiong, *et al.*, Transcriptomic and Epigenetic Profiling of Fibroblasts in Idiopathic Pulmonary Fibrosis, *Am. J. Respir. Cell Mol. Biol.*, 2022, **66**(1), 53–63.

63 L. R. Rodriguez, M. Emblom-Callahan, M. Chhina, S. Bui, B. Aljeburry, L. H. Tran, *et al.*, Global Gene Expression Analysis in an in vitro Fibroblast Model of Idiopathic Pulmonary Fibrosis Reveals Potential Role for CXCL14/CXCR4, *Sci. Rep.*, 2018, **8**(1), 3983.

64 E. T. Hoffman, F. E. Uhl, L. Asarian, B. Deng, C. Becker, J. J. Uriarte, *et al.*, Regional and disease specific human

lung extracellular matrix composition, *Biomaterials*, 2023, **293**, 121960.

65 H. Kitamura, S. Cambier, S. Somanath, T. Barker, S. Minagawa, J. Markovics, *et al.*, Mouse and human lung fibroblasts regulate dendritic cell trafficking, airway inflammation, and fibrosis through integrin αvβ8−mediated activation of TGF-β, *J. Clin. Invest.*, 2011, **121**(7), 2863–2875.